

## REVIEW SUMMARY

## NANOMATERIALS

# The world of two-dimensional carbides and nitrides (MXenes)

Armin VahidMohammadi, Johanna Rosen, Yury Gogotsi\*

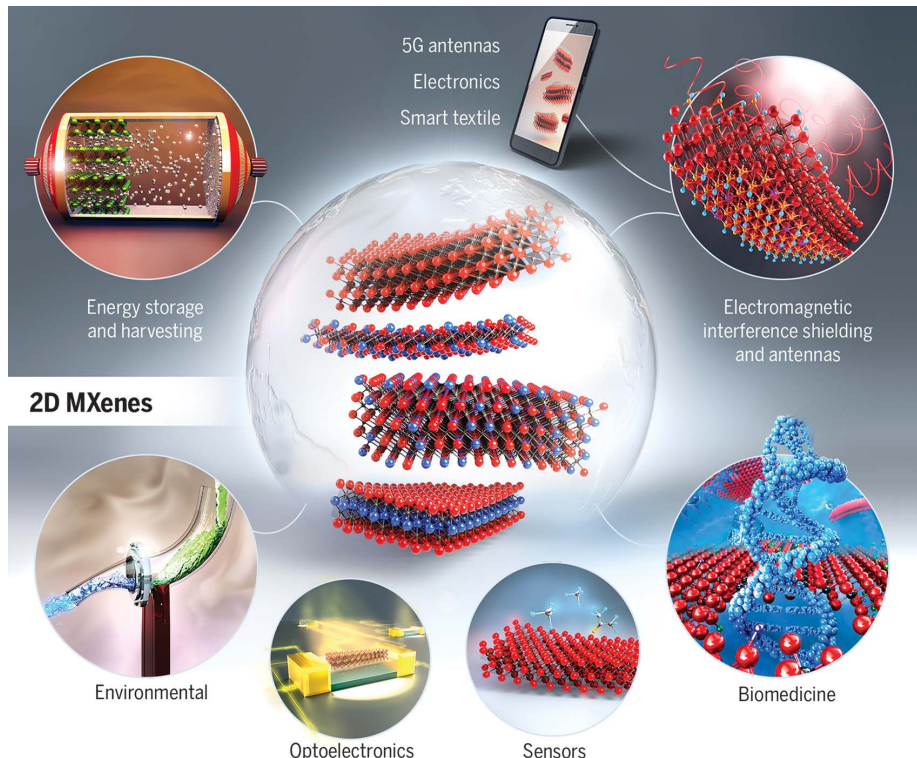
**BACKGROUND:** Appreciation of the fact that synthesis of two-dimensional (2D) materials does not necessarily require van der Waals bonded layered precursors led to discovery of many new materials, including MXenes—2D carbides and nitrides of transition metals, produced by selective etching of strongly bonded layered solids.  $Ti_3C_2$  was first reported in 2011 and set the stage for synthesis of  $Ti_2C$ ,  $Ta_4C_3$ , and other MXenes from their MAX phase precursors, demonstrating three types of possible structures ( $M_2X$ ,  $M_3X_2$ , and  $M_4X_3$ ).  $M_5C_4$  was later produced, further increasing the structural diversity and bringing the number of theoretically possible compositions to more than 100, including those with in-plane and out-of-plane ordering of the metal atoms. Con-

sidering various surface terminations of MXenes, the number of distinct compositions increases by another order of magnitude. The ability of MXenes to form carbonitrides and solid solutions suggests a potentially infinite number of compositions and opens a new era of computationally driven atomistic design of 2D materials.

**ADVANCES:** MXenes add a large number of building blocks, mainly metallic conductors, to the family of 2D materials, most of which are dielectrics, semiconductors, or semimetals. By using tunable properties of MXenes, one can build devices ranging from transistors to supercapacitors, batteries, antennas, and sensors from 2D nanosheets by using additive manufacturing or other coating and process-

ing techniques. MXenes have already shown a variety of electronic, optical, chemical, and mechanical properties, and the concept of MXetronics (all-MXene optoelectronics) has been proposed. High electronic conductivity allows their use in current collectors, interconnects, and conductive inks. MXenes possess electrochemically and chemically tunable plasmonic properties, with interband transitions and plasmon resonance peaks covering the entire ultraviolet, visible, and near-infrared range, which allow their electrochromic and photothermal therapy applications. Their strong interaction with electromagnetic waves from terahertz to gigahertz frequencies is used in electromagnetic interference shielding and communication. Redox activity of transition metal atoms on the MXene surface enables electrochemical energy storage in batteries and supercapacitors as well as electrocatalysis. Controlled spacing between the 2D sheets is used for separation of gases, water purification, and dialysis. The surface charge of MXenes allows aqueous processing without surfactants or binders as well as formation of liquid crystals. Organic molecules, polymers, and ions can be intercalated between MXene layers, allowing properties tuning and multilayer assemblies. Nontoxic and environmentally friendly titanium-based MXenes, built of abundant elements, and their hybrids and composites with polymers, ceramics, and metals are particularly attracting considerable attention.

**OUTLOOK:** While progress has been made on the preparation of carbide MXenes, synthesis of nitrides is trailing behind. Vapor phase synthesis is needed for integration of MXenes on chips using current microfabrication device technology. Large-scale, environmentally friendly synthesis methods are the key to wide use of MXenes in future additive manufacturing technologies. Precise control of the structure and surface chemistry, including defects and strain engineering, should pave the way to theoretically predicted intrinsically semiconducting, topologically insulating, and ferromagnetic MXenes as well as other discoveries in MXene physics and chemistry. Mechanically strong, environmentally stable, and highly conductive MXenes may have a major impact on flexible, printable, and wearable self-powered electronics. However, the use of MXenes in combination with other 2D materials to build heterostructures and devices by self-assembly from solution is perhaps the most exciting prospect. ■



**Structure and applications of 2D carbides and nitrides (MXenes).** The large number of MXene compositions having structures with three, five, seven, or nine atomic layers containing one or two kinds of metal atoms and various surface terminations ( $-F$ ,  $=O$ ,  $-Cl$ ,  $-Br$ , etc.) have shown promising optoelectronic, mechanical, and electrochemical properties. They have found use in a wide range of applications ranging from energy storage and harvesting to catalysis, water purification and desalination, electromagnetic interference shielding, communication, optics, electronics, plasmonics, sensors, actuators, composites, and medicine.

The list of author affiliations is available in the full article online.

\*Corresponding author. Email: gogotsi@drexel.edu

Cite this article as A. VahidMohammadi et al., *Science* **372**, eabf1581 (2021). DOI: 10.1126/science.abf1581

**S** READ THE FULL ARTICLE AT  
<https://doi.org/10.1126/science.abf1581>

## REVIEW

## NANOMATERIALS

# The world of two-dimensional carbides and nitrides (MXenes)

Armin VahidMohammadi<sup>1</sup>, Johanna Rosen<sup>2</sup>, Yury Gogotsi<sup>1\*</sup>

A decade after the first report, the family of two-dimensional (2D) carbides and nitrides (MXenes) includes structures with three, five, seven, or nine layers of atoms in an ordered or solid solution form. Dozens of MXene compositions have been produced, resulting in MXenes with mixed surface terminations. MXenes have shown useful and tunable electronic, optical, mechanical, and electrochemical properties, leading to applications ranging from optoelectronics, electromagnetic interference shielding, and wireless antennas to energy storage, catalysis, sensing, and medicine. Here we present a forward-looking review of the field of MXenes. We discuss the challenges to be addressed and outline research directions that will deepen the fundamental understanding of the properties of MXenes and enable their hybridization with other 2D materials in various emerging technologies.

**M**Xenes are a large family of two-dimensional (2D) metal carbides and nitrides having a structure consisting of two or more layers of transition metal (M) atoms packed into a honeycomb-like 2D lattice that are intervened by carbon and/or nitrogen layers (X atoms) occupying the octahedral sites between the adjacent transition metal layers (1, 2). MXenes are produced through a top-down synthesis approach, where typically A-layer atoms (e.g., Al, Si, Ga) are selectively removed from the structure of MAX phases, a group of layered, hexagonal-structure ternary carbides and nitrides (3), leaving behind loosely stacked MX layers [called “MXene” to emphasize their 2D nature (2)], which can be further separated into single-layer flakes (Fig. 1).

$Ti_3C_2T_x$  was made by selective etching of monoatomic Al layers from the  $Ti_3AlC_2$  MAX phase precursor in hydrofluoric (HF) acid (1). High metallic conductivity, hydrophilicity, and the ability to intercalate cations and store charge, demonstrated by  $Ti_3C_2T_x$  (4, 5) and other MXenes (6, 7), initially led to interest in exploring MXenes for energy storage applications. The year 2017 was the beginning of the MXenes “gold rush.” Since then, the world of 2D carbides and nitrides has been growing at an unprecedented rate. There are currently more than 30 different experimentally made stoichiometric MXenes and more than a hundred (not considering surface terminations) theoretically predicted MXenes (8–10) with distinct electronic, physical, and (electro)chemical properties. In addition, solid

solutions on M and X sides are possible, and the possibility of having multiple single (O, Cl, F, S, etc.) or mixed (O/OH/F) surface terminations makes MXenes a large and diverse family of 2D materials.

The variety of MXene structures and compositions (Fig. 1) makes it necessary to define a terminology for MXenes. The general formula of MXenes is  $M_{n+1}X_nT_x$ , where M represents the transition metal site, X represents carbon or nitrogen sites, n can vary from 1 to 4, and  $T_x$  (where x is variable) indicates surface terminations on the surface of the outer transition metal layers (8, 11). As an example, the chemical formula of a titanium carbide MXene with two layers of transition metal ( $n = 1$ ) and random terminations would be  $Ti_2CT_x$ , and a completely oxygen- or chlorine-terminated  $Ti_2CT_x$  can be written as  $Ti_2CO_2$  or  $Ti_2CCl_2$ , respectively. If there are two randomly distributed transition metals occupying M sites in the MXene structure forming a solid solution, the formula will be written as  $(M', M'')_{n+1}X_nT_x$ , where M' and M'' are two different metals [e.g.,  $(Ti, V)_2CT_x$ ]. For a specific metal composition, the concentration of each element is given in decimal numbers [e.g.,  $(Ti_{0.66}V_{0.34})_2CT_x$ ]. If the two metals have in-plane ordering and form alternating chains of M' and M'' atoms within the same M layer, the resulting MXene structure is called *i*-MXene. All *i*-MXenes known to date have a formula of  $(M'_{4/3}M''_{2/3})XT_x$ , where the concentration of each element is given as a fractional number. In most *i*-MXenes, the M'' atoms can be selectively etched, creating ordered vacancies and producing an *i*-MXene with a formula of  $M'_{4/3}XT_x$ , previously referred to as  $M'_{1.33}XT_x$ . M' and M'' atoms can also be located in separate atomic planes having an out-of-plane ordering, called *o*-MXenes, in which M'' atoms constitute the inner metal layers, and M' atoms are placed in the outer

layers. *o*-MXenes are so far known by two formulas,  $(M'_{2}M'')X_2T_x$  and  $(M'_{2}M'')_2X_3T_x$ . In addition, all MXenes can either be produced in the form of multilayer particles (*ml*-MXene) or delaminated (*d*-MXene) single-layer flakes.

## Structure and composition of MXenes

Figure 1 schematically shows the known structures of MXenes. Similar to the basal planes in the MAX phases, MXenes have a hexagonal close-packed (hcp) crystal structure with a  $P6_3/mmc$  space group symmetry, where the transition metals in the M sites are close-packed, and the X atoms occupy the octahedral sites in between the M atomic planes (11). MXenes with Ti, V, Nb, Mo, Cr, Zr, Hf, Sc, Ta, W, and Y in the M site have been reported. Note that Cr, Sc, W, or Y have only been reported as components of *o*-MXenes or *i*-MXenes, along with other metals mentioned above.

At least 26 different *o*-MXenes have been theoretically predicted (12), among which  $Mo_2Ti_2T_x$ ,  $Mo_2Sc_2T_x$ ,  $Cr_2Ti_2T_x$ , and  $Mo_2Ti_2C_3T_x$  have already been experimentally reported (13, 14). The ideal *o*-MXene composition has a ratio of M' to M'' of 2:1 or 2:2, originating from the corresponding ratios of different metal lattice sites in the MXene structure. *i*-MXenes, on the other hand, are favored only when the ratio of M' to M'' is 2:1 and the size difference between M'' and M' is at least 0.2 Å (15, 16). This requirement originates from the hexagonal atomic arrangement within the M layer, in which the M' atoms form a honeycomb lattice and the M'' atoms occupy the hexagon centers and extend out from the M layers (toward the A-layer positions in their parent *i*-MAX phase) (15). Such atomic arrangement gives *i*-MAX phases a monoclinic ( $C2/c$ ) or orthorhombic ( $C2/m$  or  $Cmcm$ ) structure, inherited by *i*-MXenes (16, 17). So far, 32 different *i*-MAX phases have been synthesized (12, 18). However, both A and M'' elements are simultaneously etched away from most *i*-MAX phases (18). For example, using HF, both Al and Sc or Y were selectively removed from  $(W_{2/3}Sc_{1/3})_2AlC$  and  $(W_{2/3}Y_{1/3})_2AlC$ , resulting in  $W_{1.33}CT_x$  *i*-MXene with ordered divacancies (19). This behavior originates from a weaker bonding of M'' elements to the carbon sites, as evidenced by their outward displacement from the M plane (20). These structural characteristics also allow the concept of targeted etching, where tuned synthesis conditions can facilitate removal of either A alone or both the A and M'' elements from the *i*-MAX phase, as shown for  $Mo_{4/3}Y_{2/3}AlC$  (20).

The X sites can be occupied by carbon, nitrogen, or both (11). Research on nitride MXenes has been limited, with the exception of *ml*- $Ti_2NT_x$  and *ml*- $Ti_4N_3T_x$  (21–23), as the synthesis of nitride MXenes presents a challenge. In carbonitride MXenes, it is believed that the C and N atoms occupy the octahedral sites randomly, independent of carbonitride stoichiometry (8).

<sup>1</sup>A.J. Drexel Nanomaterials Institute and Department of Materials Science and Engineering, Drexel University, Philadelphia, PA 19104, USA. <sup>2</sup>Department of Physics, Chemistry, and Biology (IFM), Linköping University, Linköping SE-583 31, Sweden.

\*Corresponding author. Email: gogotsi@drexel.edu

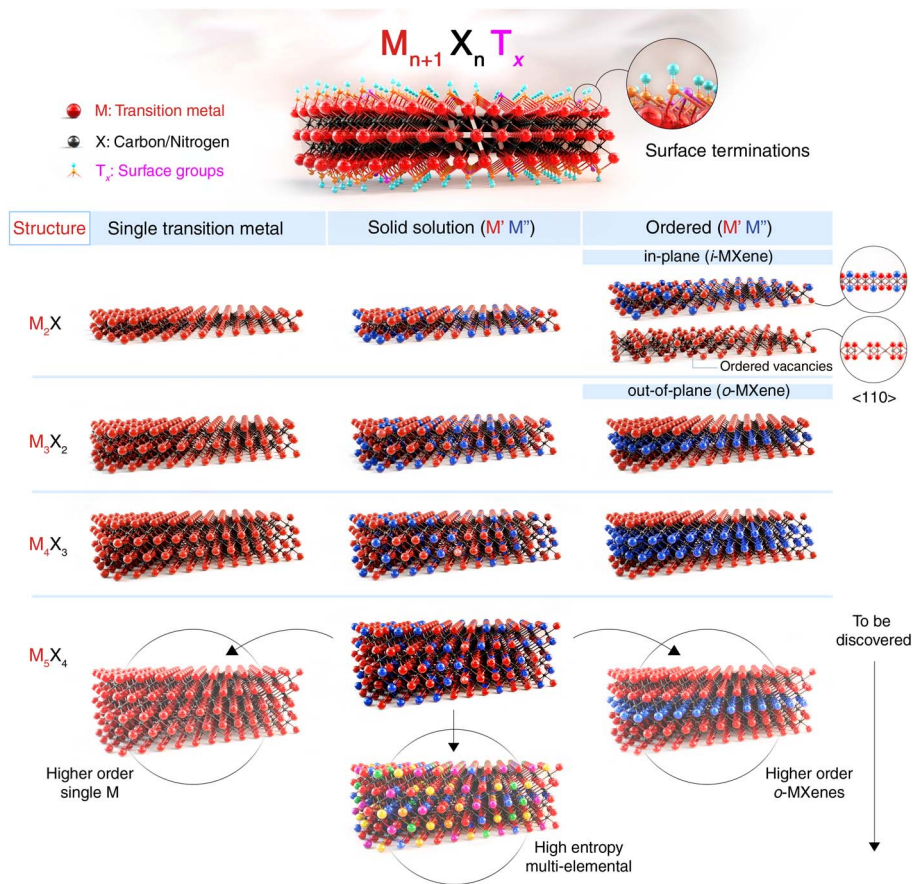


**Fig. 1. Schematic illustration of the MXene structures.** 2D MXenes have a general formula of  $M_{n+1}X_nT_x$ , where M is an early transition metal, X is carbon and/or nitrogen, and  $T_x$  represents surface terminations of the outer metal layers. The  $n$  value in the formula can vary from 1 to 4, depending on the number of transition metal layers (and carbon and/or nitrogen layers) present in the structure of MXenes, for example,  $Ti_2CT_x$  ( $n = 1$ ),  $Ti_3C_2T_x$  ( $n = 2$ ),  $Nb_4C_3T_x$  ( $n = 3$ ), and  $(Mo,V)_5C_4T_x$  ( $n = 4$ ). In contrast to all previously known MXenes, the recently discovered  $Mo_4VC_4T_x$  solid solution MXene with five M layers shows twinning in the M layers (146). The M sites of MXenes can be occupied by one or more transition metal atoms, forming solid solutions or ordered structures. The ordered double transition metal MXenes exist as in-plane ordered structures [*i*-MXenes, e.g.,  $(Mo_{2/3}Y_{1/3})_2CT_x$ ]; in-plane vacancy structures (e.g.,  $W_{2/3}CT_x$ ); and out-of-plane ordered structures (*o*-MXenes), where either one layer of M'' transition metal is sandwiched between two layers of M' transition metal (e.g.,  $Mo_2TiC_2T_x$ ) or two layers of M'' transition metals are sandwiched between two layers of M' transition metals (e.g.,  $Mo_2Ti_2C_3T_x$ ). Other arrangements, such as one or three layers of M'' sandwiched between the layers of M' (bottom row) in the  $M_5X_4$  structure, may be possible. Faded images at the bottom of the figure represent predicted structures such as high-entropy MXenes and higher-order single M or *o*-MXenes that have yet to be experimentally verified.

However, further investigations are required to provide a better understanding of the arrangement of X site atoms in these MXenes. In bulk carbides and nitrides of transition metals, oxygen can substitute for either C or N in the lattice, forming oxycarbides or oxynitrides, respectively. The possibility of such substitution in MXenes should be investigated.

The surface of MXenes (Fig. 2A) is covered with single or mixed terminations ( $T = O, OH, NH, F, Cl, Br, S, Se, Te$ ), depending on the synthesis process used and MXene composition (8, 24). These terminations can be altered or completely removed by postprocessing (24, 25), and this has a profound effect on properties.

Synthesis of MXenes in fluorine- and chlorine-containing acidic solutions results in MXenes with mixed surface terminations where the composition of  $T_x$  (surface groups) in the MXene formula can be described as  $(OH)_mO_xF_yCl_z$  (25–27). Nuclear magnetic resonance (NMR), elastic neutron scattering, x-ray photoelectron spectroscopy (XPS), and scanning transmission electron microscopy (STEM) techniques along with density functional theory (DFT) predictions have suggested a random distribution for F, OH, and O with a varying ratio, depending on the synthesis method, where F and O terminations usually dominate over OH groups in the dry state (26, 28–30). The T

atoms can reside at the surface in different positions relative to M and X atoms. The most energetically favorable and thermodynamically stable site for these moieties is on the surface of  $M_2C$ ,  $M_3C_2$ , and  $M_4C_3$  layers, centered above the transition metal atoms of the atomic plane beneath the outer layer [face-centered cubic (fcc) site] (28, 31). Functional groups can also arrange on the surface in a way that they reside on top of the X atoms (hcp sites). Although there is competition at room temperature between different groups to reside in the preferred thermodynamically stable sites, STEM studies have shown that F atoms are the ones occupying the fcc sites, whereas O atoms can reside at both sites (28). The composition and coordination of MXenes' terminations can be modified through thermal processing and vacuum annealing (28, 32, 33). For example, the surface of  $Ti_3C_2T_x$  and  $Ti_3CNT_x$  MXenes can be completely defluorinated at temperatures above 550°C (28, 32, 33).

The structure of MXenes produced using aqueous etchants contains two types of intercalated (structural) water, physisorbed and chemisorbed. The physisorbed water can be removed at temperatures below 200°C, while the monolayer of chemisorbed water with hydrogen bonding to the surface may still remain intercalated in the MXene (33, 34), requiring vacuum annealing at temperatures reaching 500°C for removal (25, 34).

Cl-terminated multilayer MXenes ( $M_{n+1}X_nCl_2$ ) can be produced by etching in Lewis acids forming  $CuCl_2$  or  $CdCl_2$  salt melts (24, 35, 36). Bro-mides, such as  $CdBr_2$ , can be used instead of  $CdCl_2$  to achieve Br terminations (24). These uniform halogen terminations (specifically Br) at the surface of MXenes can be removed to produce a collapsed 3D structure, where there is substantial interlayer interaction between the MXene sheets, similar to electrides (37). These terminations can also be exchanged with other functional groups through subsequent surface reactions, further expanding the range of MXene compositions. For example, heating of  $Ti_3C_2Br_2$  to 300°C in the presence of LiH removed surface terminations and produced multilayer  $Ti_3C_2$  (24). Similarly, MXenes with Se, Te, S, NH, and O terminations have been produced (24). Rietveld refinement, extended x-ray absorption fine structure (EXAFS), and pair distribution function (PDF) analyses have shown that the structure of MXenes slightly changes depending on the type of uniform surface terminations, resulting in in-plane compressive or tensile strain (24).

### Theory and experimental demonstration

#### of MXene properties

#### Electronic properties

The physical and (electro)chemical properties of MXenes are dependent on their composition and structure as well as their surface and

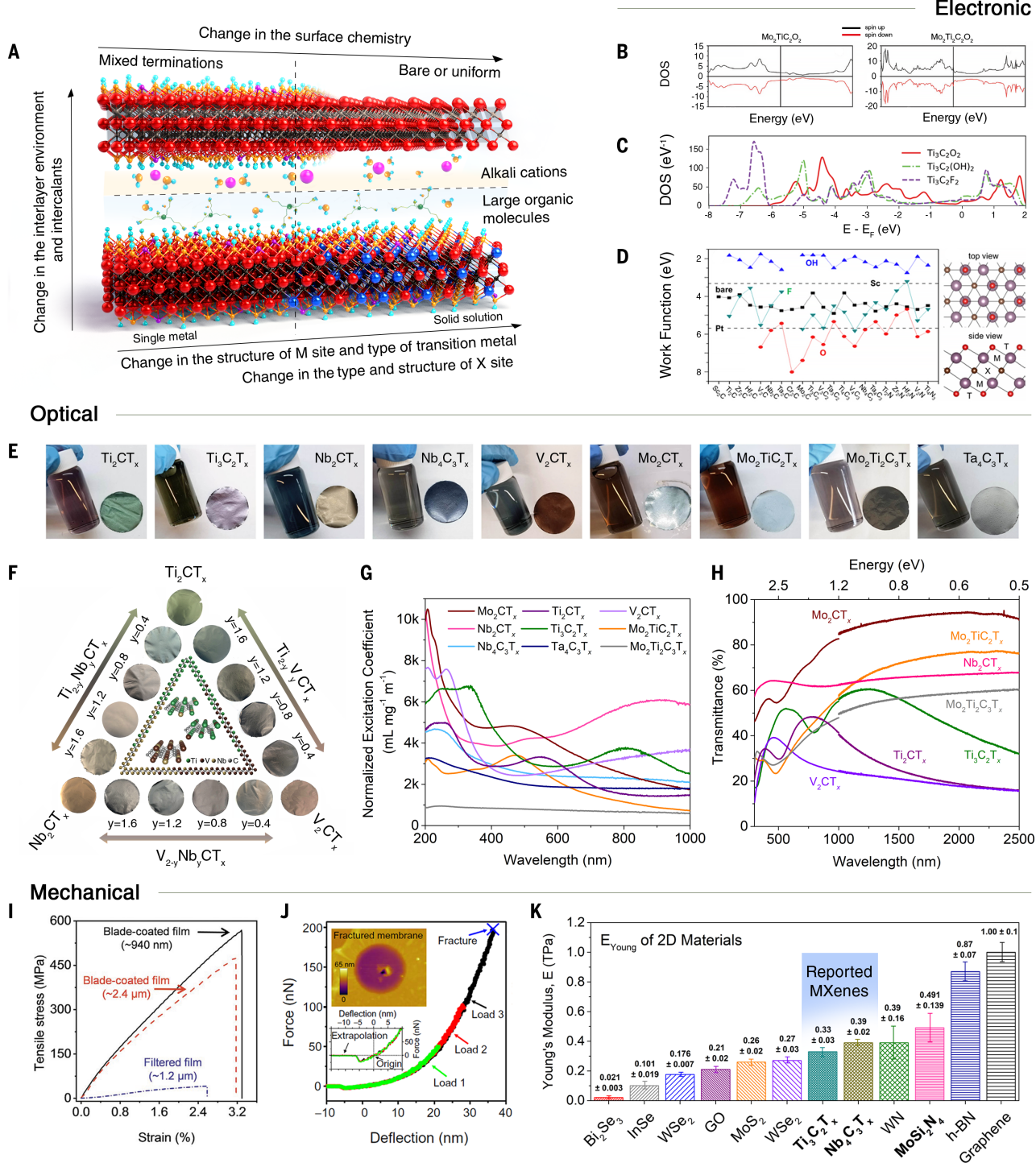


**Fig. 2. Electronic, optical, and mechanical properties of MXenes.** (A) Schematic illustration of different compositional and structural factors determining electronic and optical properties of MXenes. (B) Total DOS for  $\text{Mo}_2\text{TiC}_2\text{O}_2$  and  $\text{Mo}_2\text{Ti}_2\text{C}_2\text{O}_2$ , showing the effect of MXene structure (40). (C) DOS of  $\text{Ti}_3\text{C}_2$ ,  $\text{Ti}_3\text{C}_2\text{O}_2$ ,  $\text{Ti}_3\text{C}_2(\text{OH})_2$ , and  $\text{Ti}_3\text{C}_2\text{F}_2$ , showing the effect of surface chemistry on electronic properties of MXenes (44). (D) Dependence of the work function (eV) on their surface chemistry (45). (E) The color of colloidal solutions of various MXenes and their corresponding freestanding films (54). (F) Digital photographs of three  $\text{M}'_{2-y}\text{M}''_y\text{CT}_x$  solid solution systems, showing the change in optical properties and color of freestanding MXene films due to a gradual change in the stoichiometry (55). (G) UV-vis-NIR optical extinction properties (Normalized Excitation Coefficient) versus Wavelength (nm) for various MXenes. (H) UV-vis-NIR transmittance spectra from 300 to 2500 nm for MXene thin films (54). (I) Tensile stress versus strain curves of  $\text{Ti}_3\text{C}_2\text{T}_x$  films with different thickness produced by vacuum-assisted filtration and blade coating (60). (J) Force-deflection curves of a bilayer  $\text{Ti}_3\text{C}_2\text{T}_x$  flake at different loads. The lower inset is a detailed view of the same curves showing the center of origin. The top inset shows an AFM image of a punctured flake with no sign of catastrophic rupture (61). (K) Comparison of the effective Young's moduli of single-layer  $\text{Ti}_3\text{C}_2\text{T}_x$  and  $\text{Nb}_4\text{C}_3\text{T}_x$  with other 2D materials tested in similar nano-indentation experiments (62). [(B) to (K) adapted with permission from (40, 44, 45, 54, 55, 60–62)]

of aqueous dispersions of various 2D transition metal carbides (54). (H) UV-vis-NIR transmittance spectra from 300 to 2500 nm for MXene thin films (54). (I) Tensile stress versus strain curves of  $\text{Ti}_3\text{C}_2\text{T}_x$  films with different thickness produced by vacuum-assisted filtration and blade coating (60). (J) Force-deflection curves of a bilayer  $\text{Ti}_3\text{C}_2\text{T}_x$  flake at different loads. The lower inset is a detailed view of the same curves showing the center of origin. The top inset shows an AFM image of a punctured flake with no sign of catastrophic rupture (61). (K) Comparison of the effective Young's moduli of single-layer  $\text{Ti}_3\text{C}_2\text{T}_x$  and  $\text{Nb}_4\text{C}_3\text{T}_x$  with other 2D materials tested in similar nano-indentation experiments (62). [(B) to (K) adapted with permission from (40, 44, 45, 54, 55, 60–62)]

interlayer chemistry (Fig. 2A). The electron transport behavior of most MXenes is similar to metals, with resistivity decreasing linearly with temperature ( $\frac{dR}{dT} > 0$ ) (38, 39). However, altering the transition metal type and the structure of the M site of MXenes can result in a negative temperature dependence of resistivity ( $\frac{dR}{dT} < 0$ ) and, therefore, MXenes with semiconductor-like behavior (32, 40). Examples of the latter include  $\text{Mo}_2\text{CT}_x$ ,  $\text{Nb}_2\text{CT}_x$ , and  $\text{V}_2\text{CT}_x$  (21, 41). Moreover, while  $\text{Ti}_3\text{C}_2\text{T}_x$  has metallic conductivity,  $\text{Mo}_2\text{TiC}_2\text{T}_x$  *o*-MXene in which the outer Ti layers of  $\text{Ti}_3\text{C}_2\text{T}_x$  are substituted with Mo shows semiconductor-like behavior (40). Figure 2B shows an example of a change in the density of states (DOS) of MXenes by changing the M-site structure. Tuning the M site of *o*-MXenes by varying the outer-layer transition metals (M'') has been predicted to enable MXenes with attractive magnetic properties, primarily of antiferromagnetic character (42). Ferromagnetism has been predicted for *o*-MXenes with Mn in the middle layer and Mn nitrides (42). A magnetic glass transition in  $\text{Cr}_2\text{TiC}_2\text{T}_x$  was reported at around 30 to 35 K (43). Theoretical predictions continue to provide guidance for potential structures and compositions. For example, in some simulated *o*-MXenes, the central M'' layers are non-spin-polarized, but the M' layers at the surface are under octahedral crystal forcefields, resulting in band splitting in their 3d orbitals and, therefore, a net spin moment defining the magnetic order of the *o*-MXene (42).

All MXenes without surface terminations are predicted to be metallic conductors in which the free electrons of transition metals act as carriers (24, 39). However, surface terminations can change the DOS and shift the Fermi level, making them electronically tunable, unlike conventional metals (Fig. 2C) (44). For some MXenes other than  $\text{Ti}_3\text{C}_2\text{T}_x$ , bandgap opening and a change from metallic to semiconducting behavior has been predicted, as well as a large variation in their work functions (Fig. 2D) (39, 45). Superconductivity has been observed in  $\text{Nb}_2\text{CT}_x$  ( $T_x = \text{Se}, \text{S}$ , or NH), whereas nonterminated or O-terminated multilayer  $\text{Nb}_2\text{C}$  did not show a superconducting transition (24). MXene surface terminations also affect their thermal transport and thermoelectric properties (46). The intercalants, which are often used for delamination, also affect the electronic properties of multilayers and films (32). The intercalation of large organic cations, such as tetrabutylammonium (TBA $^+$ ), between MXene flakes results in a large interlayer spacing (47, 48), which hinders interflake electron hopping, making the produced films less conductive. In contrast, intercalated alkali cations tend to preserve a small interlayer distance and high conductivity of MXenes (49, 50). Deintercalation of water and TBA $^+$  from  $\text{Mo}_2\text{TiC}_2\text{T}_x$  and  $\text{Ti}_3\text{CNT}_x$  MXenes resulted

in a transition from ensemble semiconducting (a negative  $dR/dT$ ) to a metallic behavior (32).

The flake size, stoichiometry, surface chemistry, and point defects (mostly vacancies in the M and C sublattices either inherited from the precursor or induced by etching) also affect the physical properties of MXenes and their chemical stability (51). Larger  $\text{Ti}_3\text{C}_2\text{T}_x$  flakes with fewer defects show better intraflake electron transport and chemical stability, and their conductivity can reach 20,000 S cm $^{-1}$  (52).

### Optical properties

MXenes show longitudinal and transversal surface plasmon modes in the visible and near-infrared (vis-NIR) range, where transversal plasmons are shown to be independent of the flake's lateral dimension (38, 53). They also show strong absorption in the ultraviolet (UV) range owing to interband transitions. The optical properties of MXenes are dependent on the type and structure of the M and X sites as well as the stoichiometry of surface terminations. Different MXenes have plasmonic peaks spanning the entire vis-NIR spectrum region (54, 55) and plasmonic colors in transmission (colloidal solution or thin film) and reflection (solid-state multilayer films), as shown in Fig. 2, E and F (38). Generally, by decreasing the *n* value of MXenes, the prominent excitation peaks in their optical spectra shift to higher energies (54). For example,  $\text{Ti}_3\text{C}_2\text{T}_x$  MXene has an emerald green color in transmission and a purple color in reflection, with a characteristic absorbance peak centered at 1.6 eV [wavelength ( $\lambda$ ) of ~770 nm] (54), whereas  $\text{V}_2\text{CT}_x$  has a greenish blue color in transmission and a brownish gold color in reflection, with no absorption peak in the ultraviolet-vis-NIR (UV-vis-NIR) spectrum region (Fig. 2, G and H). The direct current conductivity to optical conductivity figure of merit for transparent  $\text{Ti}_3\text{C}_2\text{T}_x$  thin films has been reported to reach a value of 15, which is superior to that of graphene and carbon nanotubes (56), owing to the lower sheet resistance (~201 ohms per square) of  $\text{Ti}_3\text{C}_2\text{T}_x$  thin films with optical transmittance of ~87%.  $\text{V}_2\text{CT}_x$  has shown an even higher figure of merit (57). In solid solution MXenes, a change in the M':M'' ratio results in different plasmonic colors, as shown in Fig. 2F for several compositions in the  $(\text{Ti}, \text{Nb})_2\text{CT}_x$  and  $(\text{Ti}, \text{V})_2\text{CT}_x$  systems (55). Nonlinear optical behavior (decreasing transmittance with increasing light intensity) was observed for  $\text{Ti}_3\text{C}_2\text{T}_x$  thin films, explained by a plasmon-induced increase in the ground-state absorption, which results in a saturable absorption at a wavelength of 1064 nm (58).

### Mechanical properties

While the high elastic modulus of MXenes, similar to that of bulk carbides (59), was predicted in the early studies (1), experimental

exploration of mechanical properties of MXenes is just starting.  $\text{Ti}_3\text{C}_2\text{T}_x$  MXene films (thickness of ~940 nm) prepared by a blade coating technique have shown a tensile strength of ~560 MPa (Fig. 2I), which exceeds that of aluminum foil (60). In terms of fundamental mechanical properties, so far, only single-layer flakes of  $\text{Ti}_3\text{C}_2\text{T}_x$  and  $\text{Nb}_4\text{C}_3\text{T}_x$  have been experimentally tested using atomic force microscopy (AFM) nanoindentation (61, 62). Young's modulus (*E*) of single-layer  $\text{Ti}_3\text{C}_2\text{T}_x$  reached 0.33 TPa. Figure 2J shows the force-deflection curve during the AFM nanoindentation experiment on bilayer  $\text{Ti}_3\text{C}_2\text{T}_x$  (61).  $\text{Ti}_3\text{C}_2\text{T}_x$  membranes did not catastrophically fail, even upon rupture, and the sharp AFM tip only poked a hole (Fig. 2J, inset), demonstrating their high fracture toughness. In addition, the measured modulus of single-layer  $\text{Nb}_4\text{C}_3\text{T}_x$  reached ~0.39 TPa (62)—still lower than the theoretically predicted limit, because of the presence of point defects and surface terminations (63). The breaking strength of  $\text{Nb}_4\text{C}_3\text{T}_x$  reached  $26 \pm 1.6$  GPa. Figure 2K compares the reported Young's modulus values of various 2D materials (62), including the newly discovered vapor-grown  $\text{MoSi}_2\text{N}_4$  (64). Nitride-based MXenes are predicted to have a higher in-plane Young's modulus than carbide MXenes (65).

### Synthesis and processing

The strong bonding between M and A atoms in the MAX phases and layered carbides does not allow direct mechanical exfoliation of single MX layers from the MAX phases (2), even though intense shearing is known to produce multilayer MAX flakes (66). Therefore, a chemical or electrochemical selective etching approach enabled by the difference in the bonding energy and chemical reactivity of bonds in layered precursors is required (1, II). The metallic bonding between M- and A-layer atoms in many MAX phases is weaker than the ionic and/or covalent bonding present between M and X atoms (3), and therefore it can be broken using a kinetically and thermodynamically favorable chemical reaction in an etchant capable of dissolving the reaction products. Some preliminary studies suggest that the difference in interlayer bonding is crucial, while others stress the importance of the electrochemical conditions from calculated Pourbaix diagrams (67). The complexity of selective etching will require advancement of the simulation approaches, in line with the recently suggested use of high-throughput computations and machine learning methods (9, 68).

Removal of the A-layer atoms in wet chemical etching techniques and surface functionalization of formed MX layers (Fig. 3A) result in lattice expansion along the *c* axis, as evident from broadening and downshift of the x-ray diffraction (XRD) peaks corresponding to (00*l*) planes of MAX phases (2). If etching is

complete and all of the MAX phase is transformed into MXene, the corresponding XRD peaks of the MAX phase lose their intensity and ultimately disappear, being replaced by broad reflections from MXene's basal planes (8, 11). The etching results in exfoliation of 2D MX layers and their spontaneous termination with various surface functional groups, which reduce their chemical potential and increase their thermodynamic stability (8).

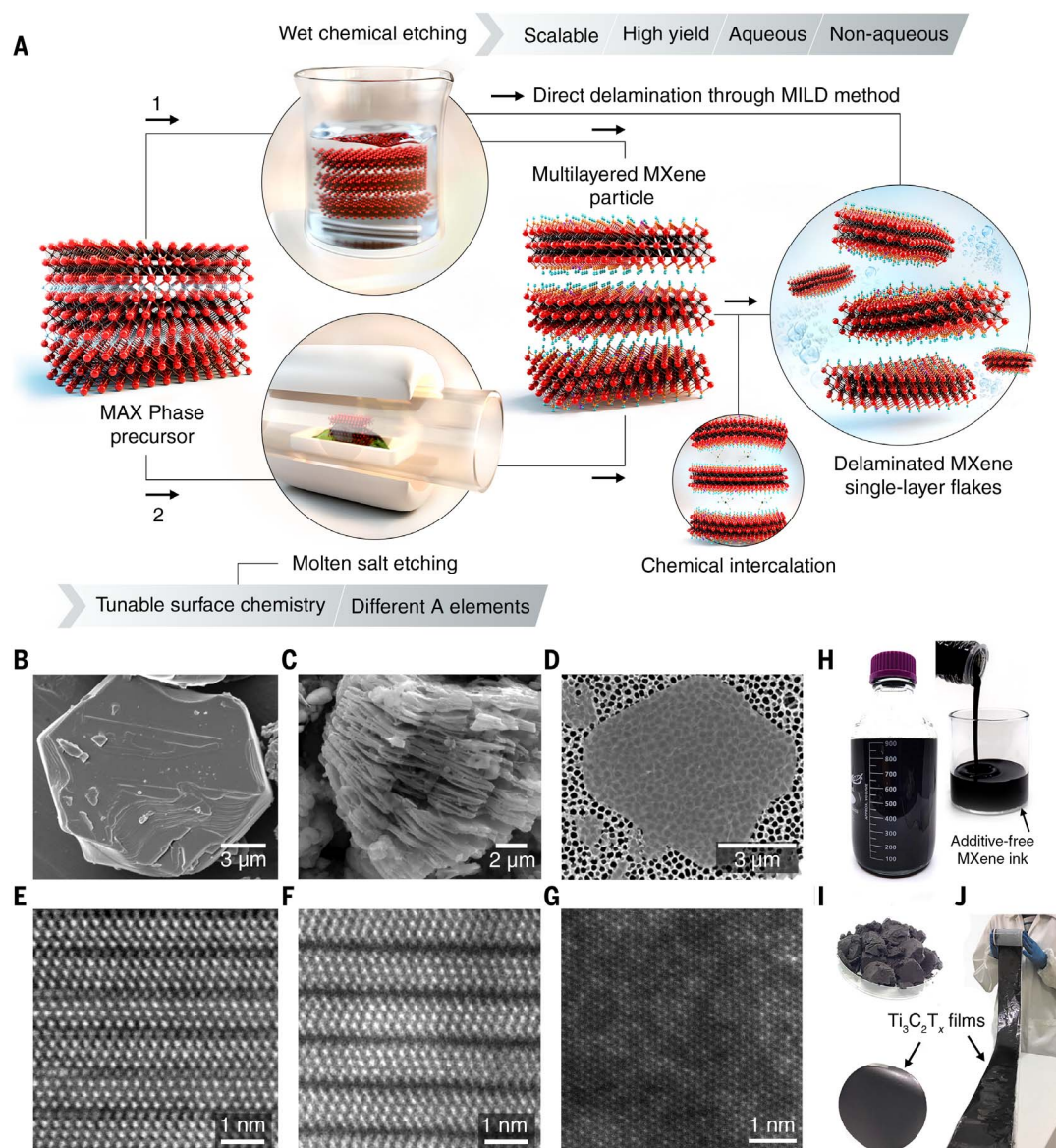
Different concentrations of HF are commonly used to etch Al-containing MAX phases (1, 8, 11). While HF has proven to be a very good etchant for selective removal of Al, it is very corrosive and poses severe health risks, which should be considered during MXene synthesis. Nevertheless, using HF as the etchant usually results in formation of *ml*-MXene particles with a signature accordion-shape mor-

phology, because of the evolution of hydrogen gas during synthesis (note that not seeing this morphology does not necessarily mean that the etching has been unsuccessful). The produced *ml*-MXenes can be subsequently delaminated into single- or few-layer flakes through chemical intercalation of organic molecules such as dimethyl sulfoxide (DMSO), tetrabutylammonium hydroxide (TBAOH), tetramethylammonium hydroxide (TMAOH), or *n*-butylamine (47, 48). Because of their anionic surface terminations, *d*-MXenes produced by wet chemical etching have a zeta potential below  $\sim 30$  mV and form stable colloidal solutions. Figure 3, B to D, shows typical morphologies of a  $\text{Ti}_3\text{AlC}_2$  MAX phase particle, *ml*- $\text{Ti}_3\text{C}_2\text{T}_x$ , and *d*- $\text{Ti}_3\text{C}_2\text{T}_x$ . Figure 3, E to G, shows STEM images of  $\text{Ti}_3\text{AlC}_2$ , *ml*- $\text{Ti}_3\text{C}_2\text{T}_x$ , and a plane-view of single-layer *d*- $\text{Ti}_3\text{C}_2\text{T}_x$  produced from it, respectively.

Etching in fluoride salts (LiF, NaF, KF, etc.) mixed with hydrochloric (HCl) or other acids is another approach that provides a safer pathway for MXene synthesis (5). In this approach, known as the MILD (minimally intensive layer delamination) method, mixing HCl and metal fluoride results in the formation of HF and an intercalant (e.g., Li ions if LiF salt is used), and therefore both etching and intercalation/delamination can be done simultaneously (69). Also, because of the presence of Li cations in between flakes, the MXene flakes produced by the MILD method show claylike rheological behavior (5, 70).  $\text{Ti}_3\text{C}_2\text{T}_x$  produced by this method does not show the accordion-like particle morphology observed in HF-etched *ml*-MXenes. Although the MILD method is applicable to just a few MXenes (15, 41, 69), it provides better control over flake size and quality (71, 72),

**Fig. 3. Synthesis and processing of MXenes.** (A) Schematic illustration of two approaches to produce MXenes by removal of A layers from MAX phases and related layered compounds. In the first approach, the MAX phase is selectively etched in fluoride ion-containing acids. By this method, multilayered MXene particles or *in situ* delaminated 2D flakes (using the MILD method) can be obtained. In the second approach, the MAX phase is selectively etched in molten salts. The product is usually multilayered MXene particles, which can then be delaminated through intercalation.

(B) Scanning electron microscope (SEM) image of a hexagonal-shape  $\text{Ti}_3\text{AlC}_2$  MAX phase crystal (52). (C) SEM image of a  $\text{Ti}_3\text{C}_2\text{T}_x$  MXene particle, derived from  $\text{Ti}_3\text{SiC}_2$  by selective etching of Si layers in molten salt (36). (D) Top-view SEM image of a delaminated  $\text{Ti}_3\text{C}_2\text{T}_x$  flake (52). (E) STEM image of a  $\text{M}_3\text{AX}_2$  MAX phase ( $\text{Ti}_3\text{AlC}_2$ ) particle. (F) The corresponding STEM image of an *ml*- $\text{M}_3\text{X}_2\text{T}_x$  MXene particle ( $\text{Ti}_3\text{C}_2\text{T}_x$ ). (G) Atomically resolved plane-view STEM image of single-layer  $\text{Ti}_3\text{C}_2\text{T}_x$  (28). (H to J) Digital photographs of  $\sim 1$  L of delaminated  $\text{Ti}_3\text{C}_2\text{T}_x$  solution (166), highly concentrated  $\text{Ti}_3\text{C}_2\text{T}_x$  ink (167), multilayered  $\text{Ti}_3\text{C}_2\text{T}_x$  MXene particles (166), a  $\text{Ti}_3\text{C}_2\text{T}_x$  film prepared by vacuum-assisted filtration of a colloidal MXene solution (168), and large-area, mechanically robust  $\text{Ti}_3\text{C}_2\text{T}_x$  film produced by blade coating (60). [(E) and (F) courtesy of P. O. Å. Persson; (B) to (D) and (G) to (J) adapted with permission from (14, 28, 36, 52, 60, 166, 167)]



producing  $Ti_3C_2T_x$  flakes with lateral dimensions of up to  $15\ \mu m$  and no pinholes (71). Etching in HF or HCl solution produces  $ml$ - $Ti_3C_2T_x$  (52, 73), which can be delaminated with LiCl instead of organic intercalants (52), resulting in higher delamination yields of ~60%. Water-free synthesis of  $Ti_3C_2T_x$  MXene in ammonium dihydrogen fluoride ( $NH_4HF_2$ ) dissolved in polar organic solvents (e.g., propylene carbonate) produces  $Ti_3C_2T_x$  with a very large interlayer spacing of 21 to 51 Å (depending on the solvent), which was attributed to co-intercalation of  $NH_4^+$  cation complexes with solvent molecules (74). Generally, water-free etchants promote chemical stability of MXene and minimize its oxidation, while elimination of fluoride-containing etchants is expected to substantially reduce the defects on MXenes and enable tunable terminations. Examples of these can be seen in two recently developed etching approaches, one using halogen compounds, i.e., tetrabutyl ammonium bromide (75) in anhydrous cyclohexane to synthesize  $Ti_3C_2Br_2$  from  $Ti_3AlC_2$ , and another using iodine in anhydrous acetonitrile ( $CH_3CN$ ) to prepare  $Ti_3C_2T_x$  with oxygen terminations (76).

Wet chemical etching techniques have produced MXenes from Al-containing MAX phases and related ceramics (non-MAX phases), with a few exceptions where Ga double-layers (77),  $[Al(Si)]_4C_4$  (78) and  $Al_3C_3$  (79) carbide layers, or Si monolayers (80) were removed using HF or a mixture of HF and oxidants, such as  $H_2O_2$ . Molten salts that form Lewis acids ( $CuCl_2$ ,  $CdCl_2$ , or  $CdBr_2$ ) can selectively etch a larger variety of A-layer elements (Al, Zn, Si, Ga, etc.) from MAX phases at moderate temperatures (24, 35, 36). In this approach (Fig. 3A), the A element (i.e., Si in  $Ti_3SiC_2$ ) is oxidized (in this case, to  $Si^{4+}$ ) by the cation ( $Cu^{2+}$ ) forming a volatile compound ( $SiCl_4$  boils at  $57.6^\circ C$ ) that is readily removed, yielding a Cl- or Br-terminated MXene (e.g.,  $Ti_3C_2Cl_2$ ) as the result of charge compensation by the anions (24, 36). Because the M-Cl or M-Br bonds on the surface of MXenes have a lower bond energy compared to M-F or M-O terminations, they can be modified or removed (24). For example,  $Ti_3C_2Br_2$  was transformed to  $Ti_3C_2Te_2$  and  $Ti_3C_2S_2$  by reaction with  $Li_2Te$  and  $Li_2S$ , respectively, in a  $CsBr/KBr/LiBr$  eutectic melt (24). Rapid synthesis of  $Ti_3C_2T_x$  (in milliseconds) through application of a megahertz frequency acoustic excitation to the  $Ti_3AlC_2$  MAX phase in LiF solution (81) is the latest effort toward cost-effective preparation of MXenes. Yet, among different developed etching techniques, the wet chemical etching of MAX phases in fluoride-containing acidic solutions results in the highest yield of MXene products and therefore remains the method of choice for large-scale manufacturing.

MXenes can be processed into various shapes and morphologies, as shown for  $Ti_3C_2T_x$  in

Fig. 3, H to J. The liquid crystalline MXene dispersions in water can be processed into fibers (82) or freestanding films using vacuum-assisted filtration or blade coating methods (60, 69), and printed into patterns with different geometries without any additives (83). Spin, dip, and spray coating techniques as well as layer-by-layer assembly, screen printing, inkjet printing, and other methods have been used to deposit MXenes onto various substrates (80, 84–87).

### Optical and electronic applications

Low sheet resistance and good transparency [0.1 to 8 kilohms per square at ~40 to 90% transmittance in the visible range (88)] make  $Ti_3C_2T_x$  thin films promising for optoelectronic applications where flexible transparent conductive electrodes (TCEs) are required, such as solar cells, liquid crystal displays (LCDs), and organic light-emitting diodes (OLEDs).  $Ti_3C_2T_x$  TCEs with ~4-nm thickness and transmittance of 91% have been used in transparent solid-state supercapacitors (56), delivering excellent volumetric capacitance. Reversible intercalation of protons or organic ions (e.g., TMAOH) into transparent  $Ti_3C_2T_x$  films results in a reversible change in their color, enabling electrochromic devices (89).

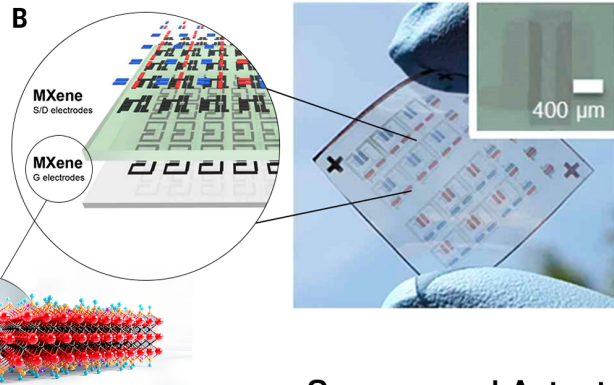
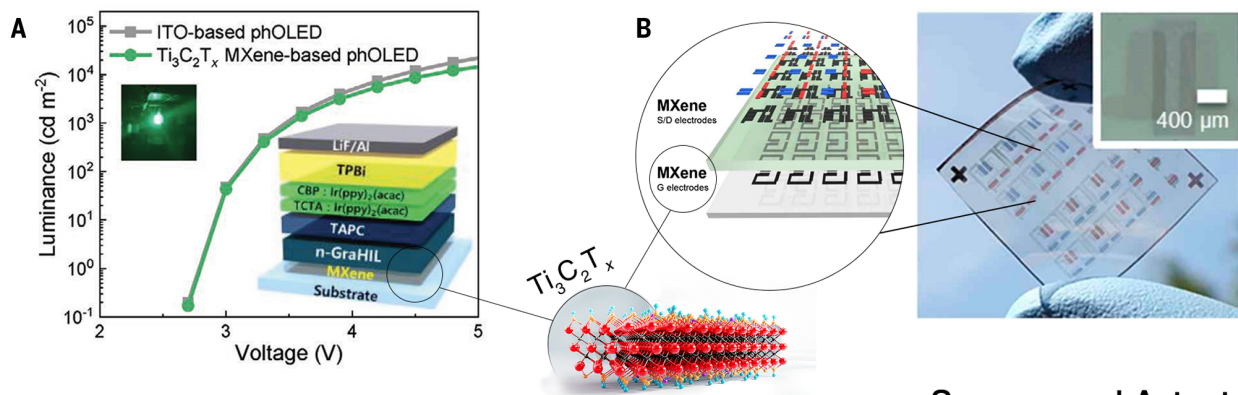
The work function of MXenes can also be tuned through modulation of their bulk and surface. For example, the  $Ti_3C_2T_x$  MXene has been predicted to have work functions ranging from ~1.81 to ~6.15 eV for completely OH- or O-terminated surface chemistries, respectively (45). The high conductivity and tunable work function promise a low energy barrier for hole injection, and this MXene has been used as TCEs in OLEDs (90) and photonic diodes (58). An OLED containing a  $Ti_3C_2T_x$  TCE (device structure is shown in the inset of Fig. 4A) with a work function tuned to 5.1 eV had external quantum efficiency of ~28.5% (90), comparable with state-of-the-art commercial OLEDs.  $Ti_3C_2T_x$  has been used in photovoltaics to tune the work function and electrode contact interfaces for an improved charge extraction process (91). For example,  $Ti_3C_2T_x$  MXene was incorporated in several components of a perovskite solar cell with a  $TiO_2$  electron transport layer, where the  $Ti_3C_2T_x$  MXene-modified perovskite solar cell showed ~5% higher power conversion efficiency (PCE) than the original cell (91). MXenes with modulated work functions have also been used as electrodes in field-effect and thin-film transistors (FET and TFT) and logic circuits (92, 93). Figure 4B shows a large array of organic FETs fabricated entirely with  $Ti_3C_2T_x$  electrodes.

Gas sensors based on MXenes can detect volatile organic compounds (VOCs) and non-polar gases, such as ammonia, ethanol, and acetone, at room temperature, mostly because of their metallic core channels and surface

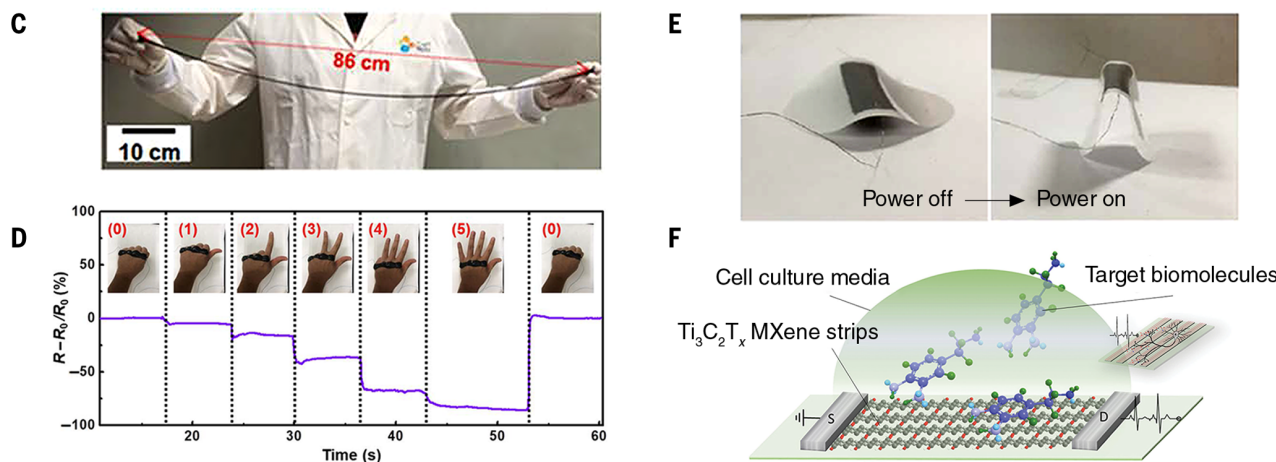
functional groups that result in strong adsorption energies for these gas molecules (94, 95). A gas sensor based on  $Ti_3C_2T_x$  delivered a two orders of magnitude greater signal-to-noise ratio and an exponential limit of detection for VOCs lower than other gas sensors based on 2D materials at room temperature (94). MXenes have also been used in biosensors (96, 97), strain sensors (98), actuators, and soft robotics (99–101). Strain sensors based on  $Ti_3C_2T_x$ -PVA (polyvinyl alcohol) hydrogels exhibited stretching of more than 3400% (Fig. 4C) and an instantaneous self-healing property with the capability of detecting complex hand gestures owing to the 3D structure of a network of MXene flakes inside the hydrogel matrix (Fig. 4D) (98). A  $Ti_3C_2T_x$ -cellulose composite soft actuator on a polycarbonate membrane showed a fast response and low-power actuation deforming up to a maximum bending angle of  $147^\circ$  at 5.1 V (Fig. 4E) (101). Electrochemical activity in various analytes, hydrophilicity, and rich surface chemistry make MXenes attractive for biosensing (Fig. 4F shows a MXene device schematic for biomolecule sensing). Freestanding MXene membranes have been used as solid-state nanopore platforms for rapid detection and translocation of single molecules (96).

High metallic conductivity and abundant free electrons are important for electromagnetic interference (EMI) shielding.  $Ti_3C_2T_x$  films of 1- to 2- $\mu m$  thickness showed an EMI shielding effectiveness (EMI SE) of ~50 dB (99.999% protection), and 92 dB at a thickness of 45  $\mu m$  (102). Various MXene compositions have been investigated for EMI shielding applications, demonstrating the role of the structure and composition of MXene in their EMI shielding properties (103). Figure 4G shows the EMI  $SE_{Total}$  of various MXenes and conventional materials versus their thickness (104). A 40- $\mu m$ -thick  $Ti_3CNT_x$  MXene film with an electronic conductivity of ~1800 S  $cm^{-1}$ , which is about one-fifth that of  $Ti_3C_2T_x$  and orders of magnitude lower than that of copper, showed an EMI  $SE_{Total}$  of 116 dB (104). Although the interaction of free electrons with incident electromagnetic waves is believed to dominate their reflection, the anomalous performance of  $Ti_3CNT_x$  films can be attributed to their layered, metamaterial-like structure (104). The fundamental reason behind this anomaly still needs to be understood. High conductivity and solution processability of  $Ti_3C_2T_x$  has also attracted attention for microwave absorbance and terahertz shielding (72), as well as wireless communication, antennas, and radio frequency identification (RFID) tags delivering comparable performances to copper antennas at a small fraction of their weight and thickness (73, 105). For example,  $Ti_3C_2T_x$  MXene patch antennas with a thickness of 5.5  $\mu m$  have shown a radiation

## Optoelectronics



## Sensors and Actuators



## Wireless and Antennas

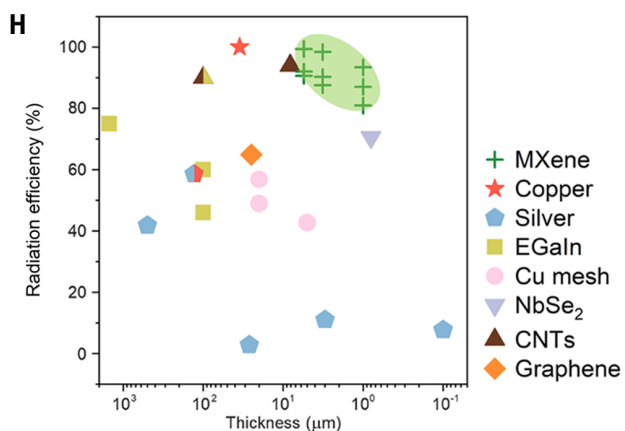
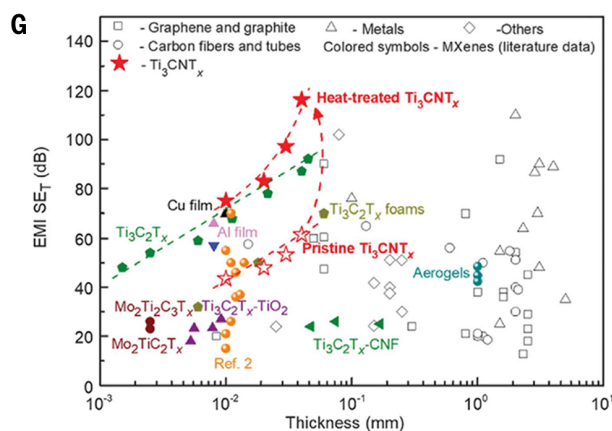


**Fig. 4. Applications of MXenes in optoelectronics, sensors and actuators, electromagnetic interference shielding, and wireless communication and antennas.** (A) Luminance of light-emitting diodes (LEDs) with indium tin oxide (ITO) and MXene transparent electrodes at different voltages. Left inset shows an optical image of a MXene-based green phosphorescent organic LED (phOLED), and the right inset shows a schematic of this device (90). (B) Photograph and device schematic of a large-scale electrode array for organic field effect transistors (OFETs) using  $\text{Ti}_3\text{C}_2\text{T}_x$  (92). (C) Photograph demonstrating the stretchability of MXene hydrogel (98). (D) Resistance change of a MXene hydrogel strain sensor in response to different hand gestures (98). (E) Response

of a  $\text{Ti}_3\text{C}_2\text{T}_x$ -cellulose soft actuator on a polycarbonate substrate to the applied voltage (101). (F) Illustration of a MXene FET with  $\text{Ti}_3\text{C}_2\text{T}_x$  electrodes for biomolecular sensing (169). (G) Comparison of EMI shielding efficiencies ( $\text{SE}_T$ ) of  $\text{Ti}_3\text{CNT}_x$ ,  $\text{Ti}_3\text{C}_2\text{T}_x$ ,  $\text{Mo}_2\text{Ti}_2\text{C}_3\text{T}_x$ , and  $\text{Mo}_2\text{TiC}_2\text{T}_x$  films with carbons and metals (104). At comparable thicknesses, the performance of annealed  $\text{Ti}_3\text{CNT}_x$  surpasses that of all other materials. (H) A comparison of radiation efficiency versus thickness for MXene patch antennas with those made of metals, carbons, and other materials (105). EGaIn, eutectic gallium-indium; CNTs, carbon nanotubes. [(A) to (H) adapted with permission from (90, 92, 98, 101, 104, 105, 169)]

efficiency of ~99% and a return loss value of -49 dB at a frequency of 16.4 GHz (105). Figure 4H compares radiation efficiency of  $Ti_3C_2T_x$  wireless antennas with that of other materials.

### Energy storage, harvesting, and electrocatalysis

The use of MXenes for electrochemical energy storage (Li-ion batteries and supercapacitors) was an early area of interest (4, 106), and we refer readers to reviews on the subject for details (8, 107). Figure 5A highlights properties of MXenes that govern their electrochemical behavior. Transition metal core layers in MXenes facilitate rapid electron transport through the electrode enabling charge storage at ultra-high rates, and a transition metal oxide-like surface provides redox-active sites for pseudocapacitive charge storage. The combination of these two properties renders MXenes promising electrode materials for ultrafast supercapacitors and batteries. In addition, subnanometer interlayer slits between 2D sheets allow rapid ion intercalation and transport, and they can be expanded through pre-intercalation, pillaring, and making hybrids or heterostructures with other 2D materials or carbon nanotubes to fit ions of different sizes (50, 85, 108, 109). The surface terminations of MXenes can be tailored toward certain redox chemistries. For example,  $Ti_3C_2I_2$  recently showed reversible high-voltage  $I^0/I^+$  redox behavior in a zinc-iodide battery (110). The electrochemical intercalation of cations with different sizes and charges from both aqueous and nonaqueous electrolytes has been observed for a variety of MXenes (4, 6, 7, 50, 111, 112). MXenes have been tested in various kinds of energy storage devices, including metal-ion, metal-sulfur, and metal-oxygen batteries. However, these materials usually have shown sloping charge-discharge profiles without a distinct plateau, typical for conventional Li- and Na-ion batteries. In Li-S (Na-S/K-S) batteries, MXenes show strong adsorption of polysulfides, high conductivity, and catalytic ability. They can also be used as a barrier for polysulfide transport on the separator, current collector, and Li host, preventing the growth of dendrites (113–115). Moreover, integrating MXenes into heterostructures with other 2D materials or hybrid architectures with high-capacity conversion-type battery materials enables battery electrodes with higher capacities, high-rate capabilities, and long cycle life. MXenes not only improve charge and ion transport inside the electrode but also can accommodate large volume expansion of the high-capacity components acting as conductive binders (109, 116, 117).

In supercapacitors,  $Ti_3C_2T_x$  electrodes deliver a volumetric and gravimetric capacitance of up to ~1500 F cm<sup>-3</sup> and ~400 F g<sup>-1</sup>, respectively, in protic H<sub>2</sub>SO<sub>4</sub> electrolyte, and thin-

film electrodes maintain more than half of their initial capacitance at 10-ms charge-discharge (118) (Fig. 5B). This shows that redox processes can be used for storage and delivery of energy at extremely high rates, as long as electronic and ionic conductivity of electrodes is sufficient. Similarly, *d*- $Mo_{4/3}CT_x$  *i*-MXene free-standing paper electrode has shown a low charge transport resistivity combined with a volumetric capacitance of 1100 F cm<sup>-3</sup> at 10 mV s<sup>-1</sup>, which was increased to ~1600 F cm<sup>-3</sup> (~700 F g<sup>-1</sup>) through post-annealing in argon (18). These results are substantially higher than for  $Mo_2CT_x$  MXene, indicating a beneficial effect of MXene vacancies on the electrochemical energy storage. In organic electrolytes, the charge storage in  $Ti_3C_2T_x$  MXene depends not only on the kind of cation but also on the solvent (119). This solvent-selective behavior is shown in Fig. 5C, where replacing the acetonitrile solvent with propylene carbonate doubled the Li<sup>+</sup> storage capacity of  $Ti_3C_2T_x$  electrode through complete desolvation of inserted Li ions (119). Consequently, proper pairing of MXenes with electrolytes is required.

As solution-processable 2D materials, MXenes can enable flexible, on-chip, printable, and wearable energy storage and harvesting devices (83, 120).  $Ti_3C_2T_x$  MXene-based microsupercapacitors prepared on different substrates, including paper, were capable of filtering high frequency ripples in AC (alternating current) line (121). Figure 5D shows a wafer-scale array of a MXene microsupercapacitor fabricated for AC-line filtering applications (121).  $Ti_3C_2T_x$ -coated conductive yarns and energy storing textiles with good environmental stability and washability have been demonstrated and used to fabricate knitted device with interdigitated electrodes (Fig. 5E).

MXenes have been used for energy harvesting and conversion applications, such as flexible triboelectric nanogenerators that can harvest energy from human motion (122, 123). The high light-to-heat conversion efficiency of  $Ti_3C_2T_x$  has rendered it one of the best materials for solar-driven water steam generation (124). Ultrasound energy harvesting has also been demonstrated (125). Moreover, lamellar freestanding  $Ti_3C_2T_x$  membranes with confined ion-selective nanofluidic channels were shown to be capable of osmotic energy harvesting under a salinity gradient (126, 127).

The oxygen atom terminations on the surface of MXenes can effectively act as the catalytic active sites for hydrogen evolution reaction (HER) (128, 129). Therefore, controlling their surface stoichiometry toward lower fluorine and higher oxygen concentrations lowers the overpotential for HER in MXenes (130). Mo-based MXenes, which have few or no fluorine terminations, show better HER performance compared with  $Ti_3C_2T_x$  or  $Ti_2CT_x$  (128, 130). Introduction of ordered vacancies, as in *i*-

MXenes, improves the performance even further, as demonstrated for  $Mo_{4/3}CT_x$  and  $W_{4/3}CT_x$  (131). Whereas in transition metal dichalcogenides (TMDS), only edges are catalytically active, the entire basal plane of MXene participates in catalysis, providing a high current density (129). The possibility of creating vacancies on M sites enables these materials to support single-atom precious metal catalysts, as demonstrated for platinum atoms immobilized on Mo-vacancies on the  $Mo_2TiC_2T_x$  surface (132). The produced catalyst showed ~40 times higher catalytical mass activity than commercially available Pt-on-carbon catalysts. MXenes have also been explored for catalyzing the oxygen evolution reaction (OER) (133) and N<sub>2</sub> reduction reactions (NRR) (134).

### Biomedical and environmental applications

Biocompatibility and low cytotoxicity of most MXene compositions, such as  $Ti_3C_2T_x$  (135),  $Nb_2CT_x$  (136), and  $Ta_4C_3T_x$  (137), as well as their plasmon resonance and high photothermal conversion efficiency in the near-IR and IR range (124) make these materials promising for cancer theranostics (Fig. 5F).  $Ta_4C_3T_x$  has attracted particular attention because of its higher photothermal efficiency (~44.7%) compared with  $Ti_3C_2T_x$  (137). Soybean phospholipid-modified  $Ta_4C_3T_x$  nanosheets were used for *in vitro* and *in vivo* photothermal ablation of breast cancer cells (137), where >90% of the MXene-incubated cells were killed upon application of a NIR laser (Fig. 5G). MXenes have also been used for drug delivery (138) and magnetic resonance imaging (MRI)-guided tumor hyperthermia applications (136).

MXenes have higher resistance to biofouling and accumulation of microorganisms and bacteria compared with graphene oxide (139) and therefore have been targeted as filtration and desalination membranes and as implantable devices.  $Ti_3C_2T_x$  was used in implantable brain electrodes with superior impedance and *in vivo* neural recording performance in comparison with gold microelectrodes (Fig. 5H) (140). Similar performance has been shown by MXene electrode arrays for high-density, high-resolution surface electromyography, where they outperformed noble metals and allowed gel-free application (141). Inspired by its exciting electro-optical properties, a  $Ti_3C_2T_x$  TCE on acrylate was explored in intraocular lenses mimicking the accommodative function of the eye's natural lens (142). Figure 5I illustrates an example of an adjustable-focus lens based on spin-coated  $Ti_3C_2T_x$  electrodes and a liquid crystal with the capability to change its refractive index (under an electric field) resulting in an optical power and change of focus (142).

The ability of  $Ti_3C_2T_x$  and  $Mo_2TiC_2T_x$  MXenes to remove urea from dialysate by adsorption is more efficient than other sorbents (143, 144)

## Energy Storage

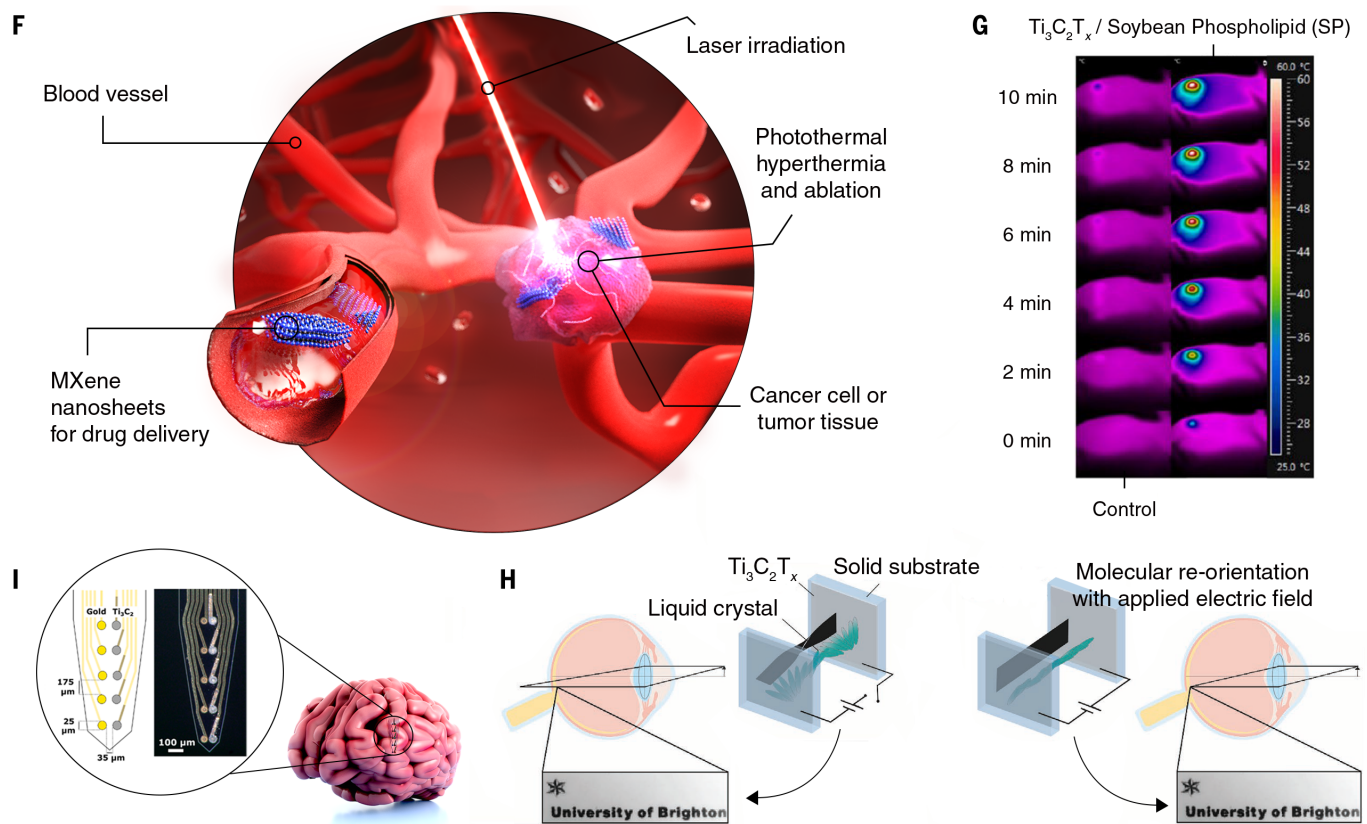
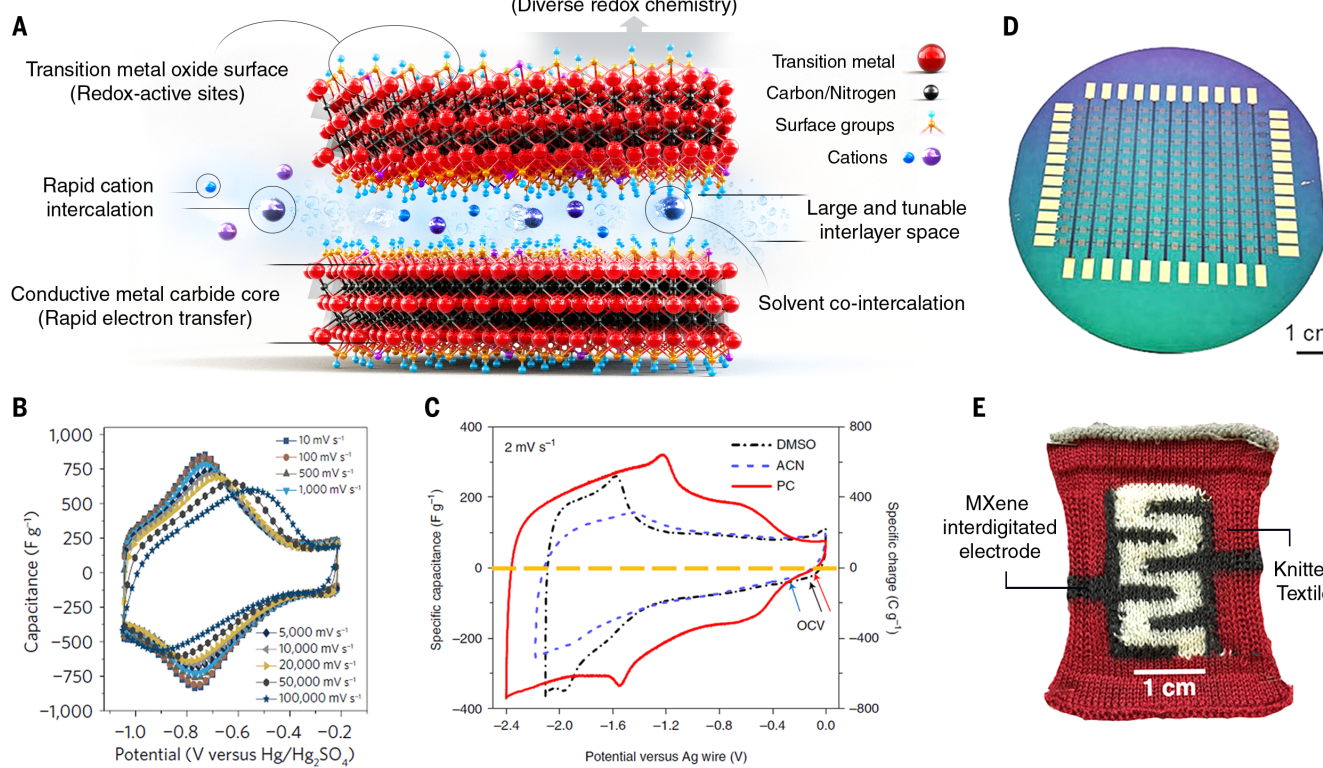


**Fig. 5. Energy storage and biomedical applications of MXenes.** (A) Schematic illustration showing MXenes' electrochemical properties for ion storage applications. (B) Cyclic voltammetry (CV) data collected at scan rates from 10 to 100,000 mV·s<sup>-1</sup> for a 90-nm-thick  $Ti_3C_2T_x$  film (118). (C) Influence of an electrolyte's solvent on the lithium-ion storage capacity of  $Ti_3C_2T_x$ ; CV curves of microporous  $Ti_3C_2T_x$  electrode in 1 M lithium bis(trifluoromethanesulfonyl)imide (LiTFSI) in DMSO, acetonitrile (ACN), or propylene carbonate (PC) electrolytes (119). (D) A digital photograph showing the wafer scale fabrication of an array of 143 MXene microsupercapacitors (121). (E) Photograph of a knitted textile with an interdigitated pattern made using  $Ti_3C_2T_x$  MXene-coated cotton yarn to produce electrodes for wearable textile supercapacitor

(170). (F) Schematic illustration of biomedical applications of MXenes. (G) Infrared thermal images of a mouse with a 4T1 tumor before and after intravenous injection of 20 mg/kg dose of  $Ti_3C_2T_x$ -soybean phospholipid under 808-nm laser irradiation (1.5 W cm<sup>-2</sup>) at different time intervals (171). (H) Schematics and bright-field microscopy image of an electrode array made from  $Ti_3C_2T_x$ /Au for brain neural activity recording (140). (I) An adjustable-focus lens constructed with glass slides coated with  $Ti_3C_2T_x$  and sandwiching a liquid crystal (LC) layer in twisted nematic orientation. Molecular reorientation of the LC layer upon application of an electric field allows focusing of the lens (142). [(D), (E), and (G) to (I) adapted with permission from (118, 119, 121, 140, 142, 170, 171)]

and may enable development of a wearable dialysis system known as an artificial kidney. The high adsorption efficiency for urea and uric toxins arises from narrow slits between functionalized and charged MXene sheets, which act as adsorption sites.

#### MXenes and beyond: Discovery and design of related 2D structures

Synthesis of *i*-MXenes, including structures with ordered vacancies; demonstration of  $Ti_4C_3$ ,  $Ti_5C_4$  (145), and  $Mo_4VC_4T_x$  MXenes (146); chemical vapor deposition (CVD) growth of nanometers-thin  $Mo_2C$  (147); synthesis of numerous solid solution MXenes; transformation of carbide MXenes into nitrides by high-temperature treatment in ammonia (148); and topochemical transformation of TMDs into 2D  $W_5N_6$  and  $Mo_5N_6$  nitrides (149) suggest the possibility of synthesis of many more 2D carbides and nitrides, which should be guided by high-throughput simulations (68) and machine learning (9) for accelerated material discovery.

Other related 2D structures with different chemical formulas, such as 2D  $MC_2$  carbides (e.g.,  $TiC_2$ —pending experimental verification) (150), vapor-grown 2D  $MoSi_2N_4$  (64), ultrathin MAX phases (MAXenes) (66), and the emerging family of 2D borides (MBenes) with a similar formula to MXenes but with boron-occupied X sites (151, 152) have been predicted, and in some cases their partially exfoliated particles have been produced or ultrathin crystals grown. Carbide and nitride electrides, such as  $Ca_2N$  (37), which have low environmental stability but attractive physical properties, are also of interest. For example, vapor-grown 2D  $MoSi_2N_4$  has a Young's modulus of ~0.5 TPa and a breaking strength of ~66 GPa (64). DFT calculations have predicted a large family of semiconducting 2D structures with a general formula of  $MA_2Z_4$ , where M is a transition metal, A is Si or Ge, and Z can be N, P, or As (64). Other calculations have predicted 2D  $MC_2$  carbides (e.g.,  $NbC_2$ ,  $TaC_2$ , and  $MoC_2$ ) for HER and OER (153), and partially etched borides have shown promise for electrocatalytic HER applications (151, 152). Similar to MAX phases, the M-A bonds in MAB phases are weaker than M-B bonds (154), potentially allowing selective etching of A-elements. However, previous

efforts only resulted in multilayer MBenes where periodic removal of Al layers forms stacking faults containing a single Al layer (only one of the Al double layers was removed during the etching from the structure of MoAlB), creating stacking sequences (i.e.,  $Mo_2AlB_2$ ) that hinder further Al deintercalation and exfoliation (151). Therefore, more research is required to identify the appropriate precursors and achieve complete exfoliation of MAB phases to MBenes.

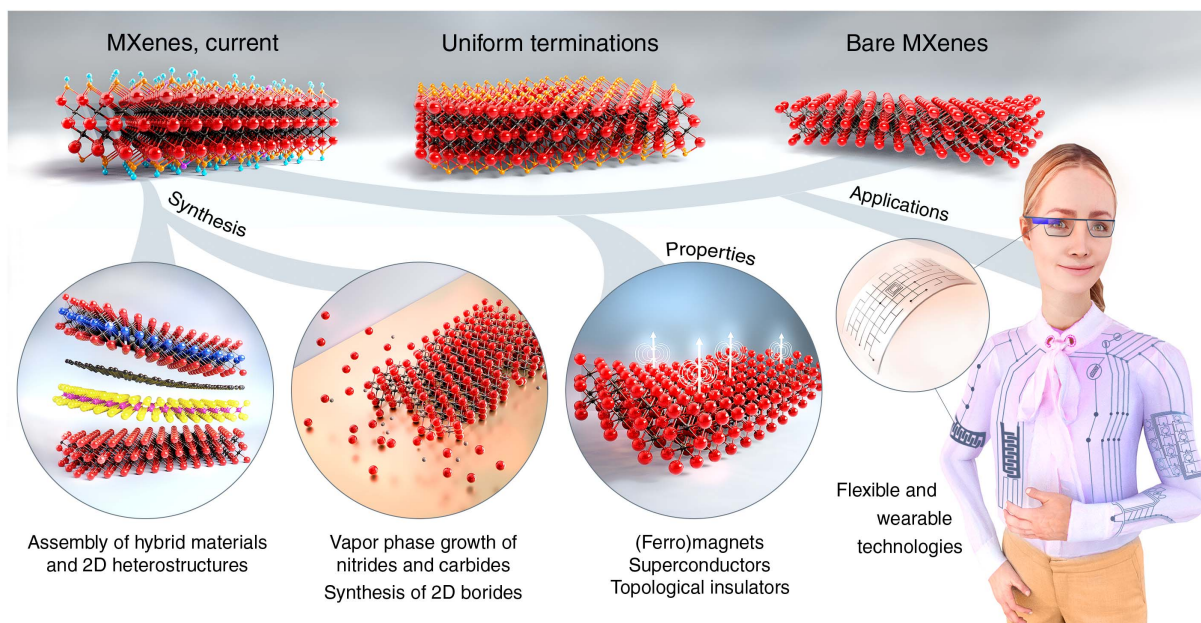
Precursors are of critical importance for MXene synthesis in general. On one hand, it is important to achieve their low-cost synthesis from ores and coal, coke, or carbon black by an Acheson-like process or self-propagating high-temperature synthesis. MXenes containing Earth-abundant elements such as Ti and carbon or nitrogen are of practical interest for large-volume applications, such as energy storage or water purification and desalination, and availability of low-cost precursors will be an enabling factor. On the other hand, synthesis of new MAX phases designed as precursors for specific MXenes is equally important, as further expansion of the family will not be possible otherwise. For example, W-containing MXene became possible because of the synthesis of W-based *i*-MAX, as W-based traditional MAX phases are not stable.  $M_5C_4$  MXene was enabled by adding a second M element. Computation-driven design of MAX phases and other precursors for MXene synthesis may assist in expansion of the family and adding new compositions and structures.

Figure 6 illustrates the potential directions for future discovery and design of 2D metal carbides, nitrides, and borides, as well as property tuning pathways that can open the possibility to move beyond the state-of-the-art and toward predicted extreme properties. Several studies have suggested tunable magnetism and ferromagnetic properties of nitride MXenes (155), which would enable MXene-based spintronic devices. In-plane chemically ordered *i*-MXenes such as those potentially originating from rare Earth (RE)-based  $Mo_{4/3}RE_{2/3}AlC$  *i*-MAX are attractive, as the magnetic elements are located at the apexes of a 2D triangular lattice, which is an arrangement that may result in a wide range of magnetic phenomena

and intricate ordered (collinear, chiral, etc.) or disordered (spin ice or liquid, etc.) ground states. Similarly, some oxygen-terminated MXenes ( $Mo$ - and Cr-containing  $M_2CO_2$  MXenes or  $Mo_2TiC_2O_2$  and  $Mo_2Ti_2O_3$  *o*-MXenes) have been predicted to be topological insulators when tailored with certain bandgaps (156, 157). The molten salt technique allows synthesis of fully oxygen-terminated MXenes and therefore may lead to experimental verification of the predicted topological insulators. Also, computationally guided synthesis and structural design approaches should be utilized to investigate the possibility of producing superconducting MXenes and enabling their use in magnetic imaging, quantum interfaces, and other applications.

#### Outlook

Over the past 10 years, the world of 2D transition metal carbides and nitrides expanded with the synthesis of  $M_5C_4T_x$ , *i*-MXenes (with or without divacancies in their basal planes), *o*-MXenes, and numerous solid solutions. Control over their physical, mechanical, and electrochemical properties via atomistic design has been demonstrated, even though ~50 MXenes reported so far constitute a small part of the family. Composition-dependent optical properties have been shown for solid solution MXenes. Reversible tuning of work function, plasmon resonance, and Fermi level by surface chemistry have been demonstrated for several MXenes. A combination of their elastic properties and mechanical strength, exceeding that of other solution-processed 2D materials, with high metallic conductivity and diverse plasmonic properties can be useful in multifunctional nanocomposites. MXenes have shown redox charge storage and delivery within milliseconds, detection of trace amounts of various gases with ultrahigh sensitivity, and the ability to adsorb urea and shield against microwave radiation. However, for predicting which MXenes will show the best radiation-shielding performance, interactions of individual nanometer-thin layers with electromagnetic waves and the related quantum effects should be considered, as continuum electrodynamics does not explain unmatched EMI shielding properties of titanium-based MXenes.



**Fig. 6. Synthesis and structural design of MXenes.** The discovery of new MXene structures and compositions, and precise control of their surface terminations, as well as their combination with other 2D materials into superlattices and 2D heterostructures, will enable emergence of new properties and expand the use of MXenes in various fields, including flexible and wearable devices for energy storage and harvesting, sensors, actuators, optical lenses, artificial memory devices, quantum computing, and Internet of Things (IoT) devices. [The base 3D model for the female character was obtained from and courtesy of [renderpeople.com](https://www.renderpeople.com)]

The use of molten salt or halogen-containing organic solvent etchants enabled synthesis of MXenes with Cl or Br terminations with the possibility to exchange them with other moieties through postprocessing. These redox-active terminated surfaces make MXenes useful in a variety of energy systems including supercapacitors and batteries, showing promise as active materials in anodes and cathodes, binders, current collectors, and electrocatalysts. Understanding the charge storage mechanisms in different MXenes, mechanisms of suppression of metal dendrite growth, dynamics of intercalation of multivalent cations ( $Mg^{2+}$ ,  $Ca^{2+}$ , or  $Al^{3+}$ ) into MXenes, and building high-power, high-energy all-MXene energy storage devices are all attractive goals.

Because of their compositional and structural variety and tailorabile properties, MXenes are now being studied in many fields, beyond what we have covered in this Review. Outstanding mechanical properties, low friction coefficient, high conductivity with the electrochemically tunable Fermi level, and optical properties make them attractive for soft robotics and actuators (101), lasers and photonics (49, 158, 159), water desalination and environmental remediation (160), (multi)functional lightweight metal-matrix (161) and ceramic-matrix composites (162), memory devices and bioinformatics (163–165), tribology, and other applications.

There are still many challenges that must be addressed to unleash the full potential of MXenes. Efficient, scalable, and cost-effective

etching techniques and delamination routes need to be developed for MXenes beyond  $Ti_3C_2T_x$ , *i*-MXenes, *o*-MXenes, and solid solution MXenes, including high-entropy ones, are of great interest owing to a wide range of possibilities in tuning their structures and properties. Nitride MXenes have been predicted to have a variety of attractive properties, from ferromagnetism to higher conductivity than carbides or semiconducting properties (155). However, only a few nitrides have been made—none of them magnetic, despite availability of their parent MAX phases. Some *o*-MXenes are expected to be topological insulators. Tunable superconductivity, large Seebeck coefficient in semiconducting MXenes, work functions ranging from 2 to 8 eV, mechanism of electron/charge transport in-plane and out-of-plane of MXenes, role of interlayer chemistry on inter-flake conduction of MXene films, electrochemical tuning of their optoelectronic behavior, and other attractive properties are to be explored. Etching routes with higher selectivity toward M-A bonds than M-N bonds should be developed to exfoliate nitride MAX phases. Beyond currently known MXenes, other 2D carbide and nitride structures, including vapor-grown 2D nitrides ( $MA_2Z_4$ ), computationally predicted  $MC_2$  carbides, and 2D borides are important targets.

It is important to mention that MXenes complement properties of other 2D materials, and they can be seen as building blocks that add metallically conductive, plasmonic, electrochemical, or catalytical properties to hybrid

materials and structures and when combined with graphene, boron nitride, dichalcogenides, and other 2D materials. This opens a path to building hybrid and heterostructure materials and devices with programmed properties using additive manufacturing and self-assembly from solution.

Methods and protocols should be established to improve the chemical stability of MXenes, especially for applications as single-layer flakes and thin films. Better understanding of the role of precursor structure and stoichiometry, as well as the etchant composition and postprocessing treatments on synthesis and properties of resulting MXenes will facilitate scale-up and large-volume manufacturing of MXenes at the commercial scale. Synthesis of MXenes from non-Al based MAX phases or MAX phase analogs must be further explored. CVD and physical vapor deposition synthesis of 2D MXenes can open the door to preparing high-quality (defect-free), large single-layer crystals, and bare MXenes, which can facilitate study of fundamental physical (quantum) properties and electronic applications of these materials in areas such as bioelectronics and electrochemical artificial synapses or neuromorphic computing.

#### REFERENCES AND NOTES

1. M. Naguib et al., Two-dimensional nanocrystals produced by exfoliation of  $Ti_3AlC_2$ . *Adv. Mater.* **23**, 4248–4253 (2011). doi: [10.1002/adma.201102306](https://doi.org/10.1002/adma.201102306); pmid: [21861270](https://pubmed.ncbi.nlm.nih.gov/21861270/)
2. M. Naguib et al., Two-dimensional transition metal carbides. *ACS Nano* **6**, 1322–1331 (2012). doi: [10.1021/nn204153h](https://doi.org/10.1021/nn204153h); pmid: [22279971](https://pubmed.ncbi.nlm.nih.gov/22279971/)

3. M. Sokol, V. Natu, S. Kota, M. W. Barsoum, On the chemical diversity of the MAX phases. *Trends Chem.* **1**, 210–223 (2019). doi: [10.1016/j.trechm.2019.02.016](https://doi.org/10.1016/j.trechm.2019.02.016)
4. M. R. Lukatskaya *et al.*, Cation intercalation and high volumetric capacitance of two-dimensional titanium carbide. *Science* **341**, 1502–1505 (2013). doi: [10.1126/science.1241488](https://doi.org/10.1126/science.1241488); pmid: [24072919](#)
5. M. Ghidiu, M. R. Lukatskaya, M. Q. Zhao, Y. Gogotsi, M. W. Barsoum, Conductive two-dimensional titanium carbide ‘clay’ with high volumetric capacitance. *Nature* **516**, 78–81 (2014). doi: [10.1038/nature13970](https://doi.org/10.1038/nature13970); pmid: [25470044](#)
6. M. Naguib *et al.*, New two-dimensional niobium and vanadium carbides as promising materials for Li-ion batteries. *J. Am. Chem. Soc.* **135**, 15966–15969 (2013). doi: [10.1021/ja405735d](https://doi.org/10.1021/ja405735d); pmid: [24144164](#)
7. X. Wang *et al.*, Pseudocapacitance of MXene nanosheets for high-power sodium-ion hybrid capacitors. *Nat. Commun.* **6**, 6544 (2015). doi: [10.1038/ncomms7544](https://doi.org/10.1038/ncomms7544); pmid: [25832913](#)
8. B. Anasori, M. R. Lukatskaya, Y. Gogotsi, 2D metal carbides and nitrides (MXenes) for energy storage. *Nat. Rev. Mater.* **2**, 16098 (2017). doi: [10.1038/natrevmats.2016.98](https://doi.org/10.1038/natrevmats.2016.98)
9. N. C. Frey *et al.*, Prediction of synthesis of 2D metal carbides and nitrides (MXenes) and their precursors with positive and unlabeled machine learning. *ACS Nano* **13**, 3031–3041 (2019). doi: [10.1021/acsnano.8b08014](https://doi.org/10.1021/acsnano.8b08014); pmid: [30830760](#)
10. B. Anasori, Y. Gogotsi, *Eds.*, **2D Metal Carbides and Nitrides (MXenes): Structure, Properties and Applications** (Springer International Publishing, 2019).
11. M. Naguib, V. N. Mochalin, M. W. Barsoum, Y. Gogotsi, 25th anniversary article: MXenes: a new family of two-dimensional materials. *Adv. Mater.* **26**, 992–1005 (2014). doi: [10.1002/adma.201304138](https://doi.org/10.1002/adma.201304138); pmid: [24357390](#)
12. W. Hong, B. C. Wyatt, S. K. Nemani, B. Anasori, Double transition-metal MXenes: Atomistic design of two-dimensional carbides and nitrides. *MRS Bull.* **45**, 850–861 (2020). doi: [10.1557/mrs.2020.251](https://doi.org/10.1557/mrs.2020.251)
13. R. Meshkian *et al.*, Theoretical stability and materials synthesis of a chemically ordered MAX phase,  $\text{Mo}_2\text{ScAlC}_2$ , and its two-dimensional derivate  $\text{Mo}_2\text{ScC}_2$  MXene. *Acta Mater.* **125**, 476–480 (2017). doi: [10.1016/j.actamat.2016.12.008](https://doi.org/10.1016/j.actamat.2016.12.008)
14. B. Anasori *et al.*, Two-dimensional, ordered, double transition metals carbides (MXenes). *ACS Nano* **9**, 9507–9516 (2015). doi: [10.1021/acsnano.5b03591](https://doi.org/10.1021/acsnano.5b03591); pmid: [26208121](#)
15. M. Dahlqvist *et al.*, Prediction and synthesis of a family of atomic laminate phases with Kagomé-like and in-plane chemical ordering. *Sci. Adv.* **3**, e1700642 (2017). doi: [10.1126/sciadv.1700642](https://doi.org/10.1126/sciadv.1700642); pmid: [28776034](#)
16. Q. Tao *et al.*, Two-dimensional  $\text{Mo}_{1.33}\text{C}$  MXene with divacancy ordering prepared from parent 3D laminate with in-plane chemical ordering. *Nat. Commun.* **8**, 14949 (2017). doi: [10.1038/ncomms14949](https://doi.org/10.1038/ncomms14949); pmid: [28440271](#)
17. A. Mockute *et al.*, Materials synthesis, neutron powder diffraction, and first-principles calculations of  $(\text{Mo}_x\text{Sc}_{1-x})_2\text{AlC}$  i-MAX phase used as parent material for MXene derivation. *Phys. Rev. Mater.* **3**, 113607 (2019). doi: [10.1103/PhysRevMaterials.3.113607](https://doi.org/10.1103/PhysRevMaterials.3.113607)
18. B. Ahmed, A. El-Ghazaly, J. Rosen, i-MXenes for energy storage and catalysis. *Adv. Funct. Mater.* **30**, 2000894 (2020). doi: [10.1002/adfm.202000894](https://doi.org/10.1002/adfm.202000894)
19. R. Meshkian *et al.*, W-based atomic laminates and their 2D derivative  $\text{W}_{1.33}\text{C}$  MXene with vacancy ordering. *Adv. Mater.* **30**, e1706409 (2018). doi: [10.1002/adma.201706409](https://doi.org/10.1002/adma.201706409); pmid: [29633399](#)
20. I. Persson *et al.*, Tailoring structure, composition, and energy storage properties of MXenes from selective etching of in-plane, chemically ordered MAX phases. *Small* **14**, e1703676 (2018). doi: [10.1002/smll.201703676](https://doi.org/10.1002/smll.201703676); pmid: [29611285](#)
21. P. Urbankowski *et al.*, Synthesis of two-dimensional titanium nitride  $\text{Ti}_4\text{N}_3$  (MXene). *Nanoscale* **8**, 11385–11391 (2016). doi: [10.1039/C6NR02253G](https://doi.org/10.1039/C6NR02253G); pmid: [27211286](#)
22. B. Soundiraraju, B. K. George, Two-dimensional titanium nitride ( $\text{Ti}_2\text{N}$ ) MXene: Synthesis, characterization, and potential application as surface-enhanced Raman scattering substrate. *ACS Nano* **11**, 8892–8900 (2017). doi: [10.1021/acsnano.7b03129](https://doi.org/10.1021/acsnano.7b03129); pmid: [28846394](#)
23. A. Djire *et al.*, Pseudocapacitive storage in nanolayered  $\text{Ti}_2\text{NT}_x$  MXene using Mg-ion electrolyte. *ACS Appl. Nano Mater.* **2**, 2785–2795 (2019). doi: [10.1021/acsnano.9b00289](https://doi.org/10.1021/acsnano.9b00289)
24. V. Kamysbayev *et al.*, Covalent surface modifications and superconductivity of two-dimensional metal carbide MXenes. *Science* **369**, 979–983 (2020). doi: [10.1126/science.aba8311](https://doi.org/10.1126/science.aba8311); pmid: [32616671](#)
25. M. Seredych *et al.*, High-temperature behavior and surface chemistry of carbide MXenes studied by thermal analysis. *Chem. Mater.* **31**, 3324–3332 (2019). doi: [10.1021/acs.chemmater.9b00397](https://doi.org/10.1021/acs.chemmater.9b00397)
26. M. A. Hope *et al.*, NMR reveals the surface functionalisation of  $\text{Ti}_3\text{C}_2$  MXene. *Phys. Chem. Chem. Phys.* **18**, 5099–5102 (2016). doi: [10.1039/C6CP00330C](https://doi.org/10.1039/C6CP00330C); pmid: [2681817](#)
27. X. Wang *et al.*, Atomic-scale recognition of surface structure and intercalation mechanism of  $\text{Ti}_3\text{C}_2\text{X}$ . *J. Am. Chem. Soc.* **137**, 2715–2721 (2015). doi: [10.1021/ja512820k](https://doi.org/10.1021/ja512820k); pmid: [25688582](#)
28. I. Persson *et al.*, On the organization and thermal behavior of functional groups on  $\text{Ti}_3\text{C}_2$  MXene surfaces in vacuum. *2D Mater.* **5**, 015002 (2018). doi: [10.1088/2053-1583/aa89cd](https://doi.org/10.1088/2053-1583/aa89cd)
29. K. J. Harris, M. Bugnet, M. Naguib, M. W. Barsoum, G. R. Goward, Direct measurement of surface termination groups and their connectivity in the 2D MXene  $\text{V}_2\text{CT}_x$  using NMR spectroscopy. *J. Phys. Chem. C* **119**, 13713–13720 (2015). doi: [10.1021/acs.jpcc.5b03038](https://doi.org/10.1021/acs.jpcc.5b03038)
30. H. W. Wang, M. Naguib, K. Page, D. J. Wesolowski, Y. Gogotsi, Resolving the structure of  $\text{Ti}_3\text{C}_2\text{T}_x$  MXenes through multilevel structural modeling of the atomic pair distribution function. *Chem. Mater.* **28**, 349–359 (2016). doi: [10.1021/acs.chemmater.5b04250](https://doi.org/10.1021/acs.chemmater.5b04250)
31. T. Schultz *et al.*, Surface termination dependent work function and electronic properties of  $\text{Ti}_{3-x}\text{C}_2\text{T}_x$  MXene. *Chem. Mater.* **31**, 6590–6597 (2019). doi: [10.1021/acs.chemmater.9b00414](https://doi.org/10.1021/acs.chemmater.9b00414)
32. J. L. Hart *et al.*, Control of MXenes' electronic properties through termination and intercalation. *Nat. Commun.* **10**, 522 (2019). doi: [10.1038/s41467-018-08169-8](https://doi.org/10.1038/s41467-018-08169-8); pmid: [30705273](#)
33. I. Persson *et al.*, How much oxygen can a MXene surface take before it breaks? *Adv. Funct. Mater.* **30**, 1909005 (2020). doi: [10.1002/adfm.201909005](https://doi.org/10.1002/adfm.201909005)
34. R. Thakur *et al.*, Insights into the thermal and chemical stability of multilayered  $\text{V}_2\text{CT}_x$  MXene. *Nanoscale* **11**, 10716–10726 (2019). doi: [10.1039/C9NR03020D](https://doi.org/10.1039/C9NR03020D); pmid: [3120085](#)
35. M. Li *et al.*, Element replacement approach by reaction with Lewis acidic molten salts to synthesize nanolaminated MAX phases and MXenes. *J. Am. Chem. Soc.* **141**, 4730–4737 (2019). doi: [10.1021/ja5b00574](https://doi.org/10.1021/ja5b00574); pmid: [30821963](#)
36. Y. Li *et al.*, A general Lewis acidic etching route for preparing MXenes with enhanced electrochemical performance in non-aqueous electrolyte. *Nat. Mater.* **19**, 894–899 (2020). doi: [10.1038/s41563-020-0657-0](https://doi.org/10.1038/s41563-020-0657-0); pmid: [32284597](#)
37. D. L. Druffel *et al.*, Experimental demonstration of an electrode as a 2D material. *J. Am. Chem. Soc.* **138**, 16089–16094 (2016). doi: [10.1021/jacs.6b10114](https://doi.org/10.1021/jacs.6b10114); pmid: [27960319](#)
38. K. Hantanasirisakul, Y. Gogotsi, Electronic and optical properties of 2D transition metal carbides and nitrides (MXenes). *Adv. Mater.* **30**, e1804779 (2018). doi: [10.1002/adma.201804779](https://doi.org/10.1002/adma.201804779); pmid: [34050752](#)
39. M. Khazaei, A. Ranjbar, M. Arai, T. Sasaki, S. Yunoki, Electronic properties and applications of MXenes: A theoretical review. *J. Mater. Chem. C* **5**, 2488–2503 (2017). doi: [10.1039/C7TC00140A](https://doi.org/10.1039/C7TC00140A)
40. B. Anasori *et al.*, Control of electronic properties of 2D carbides (MXenes) by manipulating their transition metal layers. *Nanoscale Horiz.* **1**, 227–234 (2016). doi: [10.1039/C5NH00125K](https://doi.org/10.1039/C5NH00125K); pmid: [32260625](#)
41. J. Halim *et al.*, Synthesis and characterization of 2D molybdenum carbide (MXene). *Adv. Funct. Mater.* **26**, 3118–3127 (2016). doi: [10.1002/adfm.201505328](https://doi.org/10.1002/adfm.201505328)
42. W. Sun, Y. Xie, P. R. C. Kent, Double transition metal MXenes with wide band gaps and novel magnetic properties. *Nanoscale* **10**, 11962–11968 (2018). doi: [10.1039/C8NR00513C](https://doi.org/10.1039/C8NR00513C); pmid: [29904773](#)
43. K. Hantanasirisakul *et al.*, Evidence of a magnetic transition in atomically thin  $\text{Cr}_2\text{TiC}_2\text{T}_x$  MXene. *Nanoscale Horiz.* **5**, 1557–1565 (2020). doi: [10.1039/DONH00343C](https://doi.org/10.1039/DONH00343C); pmid: [33089267](#)
44. N. M. Caffrey, Effect of mixed surface terminations on the structural and electrochemical properties of two-dimensional  $\text{Ti}_3\text{C}_2\text{T}_2$  and  $\text{V}_2\text{CT}_2$  MXenes multilayers. *Nanoscale* **10**, 13520–13530 (2018). doi: [10.1039/C8NR03221A](https://doi.org/10.1039/C8NR03221A); pmid: [2997202](#)
45. Y. Liu, H. Xiao, W. A. Goddard 3rd, Schottky-barrier-free contacts with two-dimensional semiconductors by surface-engineered MXenes. *J. Am. Chem. Soc.* **138**, 15853–15856 (2016). doi: [10.1021/ja5b10834](https://doi.org/10.1021/ja5b10834); pmid: [27960324](#)
46. M. Khazaei, M. Arai, T. Sasaki, M. Estili, Y. Sakka, Two-dimensional molybdenum carbides: Potential thermoelectric materials of the MXene family. *Phys. Chem. Chem. Phys.* **16**, 7841–7849 (2014). doi: [10.1039/C4CP00467A](https://doi.org/10.1039/C4CP00467A); pmid: [24643873](#)
47. M. Naguib, R. R. Uncic, B. L. Armstrong, J. Nanda, Large-scale delamination of multi-layers transition metal carbides and carbonitrides “MXenes”. *Dalton Trans.* **44**, 9353–9358 (2015). doi: [10.1039/C5DT01247C](https://doi.org/10.1039/C5DT01247C); pmid: [25912071](#)
48. O. Mashtalar *et al.*, Intercalation and delamination of layered carbides and carbonitrides. *Nat. Commun.* **4**, 1716 (2013). doi: [10.1038/ncomms2664](https://doi.org/10.1038/ncomms2664); pmid: [23591883](#)
49. L. Wu *et al.*, MXene-based nonlinear optical information converter for all-optical modulator and switcher. *Laser Photonics Rev.* **12**, 1800215 (2018). doi: [10.1002/lpor.201800215](https://doi.org/10.1002/lpor.201800215)
50. A. VahidMohammadi, M. Mojtabavi, N. M. Caffrey, M. Wanunu, M. Beidaghi, Assembling 2D MXenes into highly stable pseudocapacitive electrodes with high power and energy densities. *Adv. Mater.* **31**, 1806931 (2019). doi: [10.1002/adma.201806931](https://doi.org/10.1002/adma.201806931)
51. K. Maleski, C. E. Ren, M. Q. Zhao, B. Anasori, Y. Gogotsi, Size-dependent physical and electrochemical properties of two-dimensional MXene flakes. *ACS Appl. Mater. Interfaces* **10**, 24491–24498 (2018). doi: [10.1021/acsami.8b04662](https://doi.org/10.1021/acsami.8b04662); pmid: [2956920](#)
52. T. S. Mathis *et al.*, Modified MAX phase synthesis for environmentally stable and highly conductive  $\text{Ti}_3\text{C}_2$  MXene. *ACS Nano* **15**, 6420–6429 (2021). doi: [10.1021/acsnano.0c08357](https://doi.org/10.1021/acsnano.0c08357); pmid: [33848136](#)
53. J. K. El-Demellawy, S. Lopatin, J. Yin, O. F. Mohammed, H. N. Alshareef, Tunable multipolar surface plasmons in 2D  $\text{Ti}_3\text{C}_2\text{T}_x$  MXene flakes. *ACS Nano* **12**, 8485–8493 (2018). doi: [10.1021/acsnano.8b04029](https://doi.org/10.1021/acsnano.8b04029); pmid: [30020767](#)
54. K. Maleski, C. E. Shuck, A. T. Fafarman, Y. Gogotsi, The broad chromatic range of two-dimensional transition metal carbides. *Adv. Opt. Mater.* **9**, 2001563 (2020). doi: [10.1002/adom.202001563](https://doi.org/10.1002/adom.202001563)
55. M. Han *et al.*, Tailoring electronic and optical properties of MXenes through forming solid solutions. *J. Am. Chem. Soc.* **142**, 19110–19118 (2020). doi: [10.1021/jacs.0c07395](https://doi.org/10.1021/jacs.0c07395); pmid: [33108178](#)
56. C. J. Zhang *et al.*, Transparent, flexible, and conductive 2D titanium carbide (MXene) films with high volumetric capacitance. *Adv. Mater.* **29**, 1702678 (2017). doi: [10.1002/adma.201702678](https://doi.org/10.1002/adma.201702678); pmid: [28741695](#)
57. G. Ying, S. Kota, A. D. Dillon, A. T. Fafarman, M. W. Barsoum, Conductive transparent  $\text{V}_2\text{CT}_x$  (MXene) films. *FlatChem* **8**, 25–30 (2018). doi: [10.1016/j.flatc.2018.03.001](https://doi.org/10.1016/j.flatc.2018.03.001)
58. Y. Dong *et al.*, Saturable absorption in 2D  $\text{Ti}_3\text{C}_2$  MXene thin films for passive photonic diodes. *Adv. Mater.* **30**, 1705714 (2018). doi: [10.1002/adma.201705714](https://doi.org/10.1002/adma.201705714)
59. Y. G. Gogotsi, R. A. Andrievski, *Materials Science of Carbides, Nitrides and Borides* (Springer, 1999).
60. J. Zhang *et al.*, Scalable manufacturing of free-standing, strong  $\text{Ti}_3\text{C}_2\text{T}_x$  MXene films with outstanding conductivity. *Adv. Mater.* **32**, 2001093 (2020). doi: [10.1002/adma.202001093](https://doi.org/10.1002/adma.202001093)
61. A. Lipatov *et al.*, Elastic properties of 2D  $\text{Ti}_3\text{C}_2\text{T}_x$  MXene monolayers and bilayers. *Sci. Adv.* **4**, eaat0491 (2018). doi: [10.1126/sciadv.aat0491](https://doi.org/10.1126/sciadv.aat0491); pmid: [29922719](#)
62. A. Lipatov *et al.*, Electrical and elastic properties of individual single-layer  $\text{Nb}_4\text{C}_3\text{T}_x$  MXene flakes. *Adv. Electron. Mater.* **6**, 1901382 (2020). doi: [10.1002/aelm.201901382](https://doi.org/10.1002/aelm.201901382)
63. G. Plummer, B. Anasori, Y. Gogotsi, G. J. Tucker, Nanoindentation of monolayer  $\text{Ti}_{n+1}\text{C}_n\text{T}_x$  MXenes via atomistic simulations: The role of composition and defects on strength. *Comput. Mater. Sci.* **157**, 168–174 (2019). doi: [10.1016/j.commatsci.2018.10.033](https://doi.org/10.1016/j.commatsci.2018.10.033)
64. Y.-L. Hong *et al.*, Chemical vapor deposition of layered two-dimensional  $\text{MoSi}_2\text{N}_4$  materials. *Science* **369**, 670–674 (2020). doi: [10.1126/science.abb7023](https://doi.org/10.1126/science.abb7023); pmid: [32764066](#)
65. N. Zhang, Y. Hong, S. Yazdanparast, M. A. Zaeem, Superior structural, elastic and electronic properties of 2D titanium nitride MXenes over carbide MXenes: A comprehensive first principles study. *2D Mater.* **5**, 045004 (2018). doi: [10.1088/2053-1583/aactfb3](https://doi.org/10.1088/2053-1583/aactfb3)
66. K. V. Mahesh, R. Rashada, M. Kiran, A. Peer Mohamed, S. Ananthakumar, Shear induced micromechanical synthesis of  $\text{Ti}_3\text{SiC}_2$  MAXene nanosheets for functional applications. *RSC Advances* **5**, 51242–51247 (2015). doi: [10.1039/C5RA07756G](https://doi.org/10.1039/C5RA07756G)
67. C. Zhan, W. Sun, Y. Xie, D. E. Jiang, P. R. C. Kent, Computational discovery and design of MXenes for energy

- applications: Status, successes, and opportunities. *ACS Appl. Mater. Interfaces* **11**, 24885–24905 (2019). doi: [10.1021/acsmi.9b00439](https://doi.org/10.1021/acsmi.9b00439); pmid: [31082189](https://pubmed.ncbi.nlm.nih.gov/31082189/)
68. T. L. Tan, H. M. Jin, M. B. Sullivan, B. Anasori, Y. Gogotsi, High-throughput survey of ordering configurations in MXene alloys across compositions and temperatures. *ACS Nano* **11**, 4407–4418 (2017). doi: [10.1021/acsnano.6b08227](https://doi.org/10.1021/acsnano.6b08227); pmid: [28297600](https://pubmed.ncbi.nlm.nih.gov/28297600/)
  69. M. Alhabeb et al., Guidelines for synthesis and processing of two-dimensional titanium carbide ( $Ti_3C_2T_x$  MXene). *Chem. Mater.* **29**, 7633–7644 (2017). doi: [10.1021/acs.chemmater.7b02847](https://doi.org/10.1021/acs.chemmater.7b02847)
  70. B. Akuzum et al., Rheological characteristics of 2D titanium carbide (MXene) dispersions: A guide for processing MXenes. *ACS Nano* **12**, 2685–2694 (2018). doi: [10.1021/acsnano.7b08889](https://doi.org/10.1021/acsnano.7b08889); pmid: [29463080](https://pubmed.ncbi.nlm.nih.gov/29463080/)
  71. A. Lipatov et al., Effect of synthesis on quality, electronic properties and environmental stability of individual monolayer  $Ti_3C_2$  MXene flakes. *Adv. Electron. Mater.* **2**, 1600255 (2016). doi: [10.1021/aelm.201600255](https://doi.org/10.1021/aelm.201600255)
  72. G. Choi et al., Enhanced terahertz shielding of MXenes with nano-metamaterials. *Adv. Opt. Mater.* **6**, 1701076 (2018). doi: [10.1002/adom.201701076](https://doi.org/10.1002/adom.201701076)
  73. A. Sarycheva et al., 2D titanium carbide (MXene) for wireless communication. *Sci. Adv.* **4**, eaau0920 (2018). doi: [10.1126/sciadv.aau0920](https://doi.org/10.1126/sciadv.aau0920); pmid: [3025151](https://pubmed.ncbi.nlm.nih.gov/3025151/)
  74. V. Natu et al., 2D  $Ti_3C_2T_x$  MXene synthesized by water-free etching of  $Ti_3AlC_2$  in polar organic solvents. *Chem.* **6**, 616–630 (2020). doi: [10.1016/j.chempr.2020.01.019](https://doi.org/10.1016/j.chempr.2020.01.019)
  75. A. Jawaid et al., Halogen etch of  $Ti_3AlC_2$  MAX phase for MXene fabrication. *ACS Nano* **15**, 2771–2771 (2021). doi: [10.1021/acsnano.0c08630](https://doi.org/10.1021/acsnano.0c08630); pmid: [33502839](https://pubmed.ncbi.nlm.nih.gov/33502839/)
  76. H. Shi et al., Ambient-stable two-dimensional titanium carbide (MXene) enabled by iodine etching. *Angew. Chem. Int. Ed.* **60**, 8689–8693 (2021). doi: [10.1002/anie.202015627](https://doi.org/10.1002/anie.202015627); pmid: [33484049](https://pubmed.ncbi.nlm.nih.gov/33484049/)
  77. R. Meshkian et al., Synthesis of two-dimensional molybdenum carbide,  $Mo_2C$ , from the gallium based atomic laminate  $Mo_2Ga_2C$ . *Scr. Mater.* **108**, 147–150 (2015). doi: [10.1016/j.scriptamat.2015.07.003](https://doi.org/10.1016/j.scriptamat.2015.07.003)
  78. J. Zhou et al., Synthesis and electrochemical properties of two-dimensional hafnium carbide. *ACS Nano* **11**, 3841–3850 (2017). doi: [10.1021/acsnano.7b00030](https://doi.org/10.1021/acsnano.7b00030); pmid: [28375599](https://pubmed.ncbi.nlm.nih.gov/28375599/)
  79. J. Zhou et al., A two-dimensional zirconium carbide by selective etching of  $Al_3C_3$  from nanolaminated  $Zr_3Al_3C_5$ . *Angew. Chem. Int. Ed.* **55**, 5008–5013 (2016). doi: [10.1002/ange.20150432](https://doi.org/10.1002/ange.20150432); pmid: [26959082](https://pubmed.ncbi.nlm.nih.gov/26959082/)
  80. M. Alhabeb et al., Selective etching of silicon from  $Ti_3SiC_2$  (MAX) to obtain 2D titanium carbide (MXene). *Angew. Chem. Int. Ed.* **57**, 5444–5448 (2018). doi: [10.1002/anie.201802232](https://doi.org/10.1002/anie.201802232); pmid: [29518271](https://pubmed.ncbi.nlm.nih.gov/29518271/)
  81. A. E. Ghazaly et al., Ultrafast, one-step, salt-solution-based acoustic synthesis of  $Ti_3C_2$  MXene. *ACS Nano* **15**, 4287–4293 (2021). pmid: [33635629](https://pubmed.ncbi.nlm.nih.gov/33635629/)
  82. J. Zhang et al., Additive-free MXene liquid crystals and fibers. *ACS Cent. Sci.* **6**, 254–265 (2020). doi: [10.1021/acscentsci.9b01217](https://doi.org/10.1021/acscentsci.9b01217); pmid: [32123744](https://pubmed.ncbi.nlm.nih.gov/32123744/)
  83. C. J. Zhang et al., Additive-free MXene inks and direct printing of micro-supercapacitors. *Nat. Commun.* **10**, 1795 (2019). doi: [10.1038/s41467-019-10938-1](https://doi.org/10.1038/s41467-019-10938-1); pmid: [30996244](https://pubmed.ncbi.nlm.nih.gov/30996244/)
  84. H. Huang et al., Scalable, and low-cost treating-cutting-coating manufacture platform for MXene-based on-chip micro-supercapacitors. *Nano Energy* **69**, 104431 (2020). doi: [10.1016/j.nanoen.2019.104431](https://doi.org/10.1016/j.nanoen.2019.104431)
  85. W. Tian et al., Layer-by-layer self-assembly of pillared two-dimensional multilayers. *Nat. Commun.* **10**, 2558 (2019). doi: [10.1038/s41467-019-10631-0](https://doi.org/10.1038/s41467-019-10631-0); pmid: [3186411](https://pubmed.ncbi.nlm.nih.gov/3186411/)
  86. H. An et al., Surface-agnostic highly stretchable and bendable conductive MXene multilayers. *Sci. Adv.* **4**, eaao0118 (2018). doi: [10.1126/sciadv.aao0118](https://doi.org/10.1126/sciadv.aao0118); pmid: [29536044](https://pubmed.ncbi.nlm.nih.gov/29536044/)
  87. M. Mojtabavi et al., Wafer-scale lateral self-assembly of mosaic  $Ti_3C_2T_x$  MXene monolayer films. *ACS Nano* **15**, 625–636 (2021). doi: [10.1021/acsnano.0c06393](https://doi.org/10.1021/acsnano.0c06393); pmid: [33405898](https://pubmed.ncbi.nlm.nih.gov/33405898/)
  88. K. Hantanasirikul et al., Fabrication of  $Ti_3C_2T_x$  MXene transparent thin films with tunable optoelectronic properties. *Adv. Electron. Mater.* **2**, 1600050 (2016). doi: [10.1002/aelm.201600050](https://doi.org/10.1002/aelm.201600050)
  89. K. Hantanasirikul et al., Effects of synthesis and processing on optoelectronic properties of titanium carbonitride MXene. *Chem. Mater.* **31**, 2941–2951 (2019). doi: [10.1021/acs.chemmater.9b00401](https://doi.org/10.1021/acs.chemmater.9b00401)
  90. S. Ahn et al., A 2D titanium carbide MXene flexible electrode for high-efficiency light-emitting diodes. *Adv. Mater.* **32**, e2000919 (2020). doi: [10.1002/adma.2020000919](https://doi.org/10.1002/adma.2020000919); pmid: [32350958](https://pubmed.ncbi.nlm.nih.gov/32350958/)
  91. A. Agresti et al., Titanium-carbide MXenes for work function and interface engineering in perovskite solar cells. *Nat. Mater.* **18**, 1228–1234 (2019). doi: [10.1038/s41563-019-0478-1](https://doi.org/10.1038/s41563-019-0478-1); pmid: [31501556](https://pubmed.ncbi.nlm.nih.gov/31501556/)
  92. B. Lyu et al., Large-area MXene electrode array for flexible electronics. *ACS Nano* **13**, 11392–11400 (2019). doi: [10.1021/acsnano.9b04731](https://doi.org/10.1021/acsnano.9b04731); pmid: [31553884](https://pubmed.ncbi.nlm.nih.gov/31553884/)
  93. Z. Wang, H. Kim, H. N. Alshareef, Oxide thin-film electronics using all-MXene electrical contacts. *Adv. Mater.* **30**, e1706656 (2018). doi: [10.1002/adma.201706656](https://doi.org/10.1002/adma.201706656); pmid: [29473236](https://pubmed.ncbi.nlm.nih.gov/29473236/)
  94. S. J. Kim et al., Metallic  $Ti_3C_2T_x$  mxene gas sensors with ultrahigh signal-to-noise ratio. *ACS Nano* **12**, 986–993 (2018). doi: [10.1021/acsnano.7b07460](https://doi.org/10.1021/acsnano.7b07460); pmid: [29368519](https://pubmed.ncbi.nlm.nih.gov/29368519/)
  95. E. Lee et al., Room temperature gas sensing of two-dimensional titanium carbide (MXene). *ACS Appl. Mater. Interfaces* **9**, 37184–37190 (2017). doi: [10.1021/acsmi.7b1055](https://doi.org/10.1021/acsmi.7b1055); pmid: [28953355](https://pubmed.ncbi.nlm.nih.gov/28953355/)
  96. M. Mojtabavi, A. VahidMohammadi, W. Liang, M. Beidaghi, M. Wanunu, Single-molecule sensing using nanopores in two-dimensional transition metal carbide (MXene) membranes. *ACS Nano* **13**, 3042–3053 (2019). doi: [10.1021/acsnano.8b08017](https://doi.org/10.1021/acsnano.8b08017); pmid: [30844249](https://pubmed.ncbi.nlm.nih.gov/30844249/)
  97. L. Wu et al., 2D transition metal carbide MXene as a robust biosensing platform for enzyme immobilization and ultrasensitive detection of phenol. *Biosens. Bioelectron.* **107**, 69–75 (2018). doi: [10.1016/j.bios.2018.02.021](https://doi.org/10.1016/j.bios.2018.02.021); pmid: [29448223](https://pubmed.ncbi.nlm.nih.gov/29448223/)
  98. Y. Z. Zhang et al., MXenes stretch hydrogel sensor performance to new limits. *Sci. Adv.* **4**, eaat0098 (2018). doi: [10.1126/sciadv.aat0098](https://doi.org/10.1126/sciadv.aat0098); pmid: [29922718](https://pubmed.ncbi.nlm.nih.gov/29922718/)
  99. S. Umrao et al., MXene artificial muscles based on ionically cross-linked  $Ti_3C_2T_x$  electrode for kinetic soft robotics. *Sci. Robot.* **4**, eaaw7797 (2019). doi: [10.1126/scirobotics.aww7797](https://doi.org/10.1126/scirobotics.aww7797); pmid: [33137782](https://pubmed.ncbi.nlm.nih.gov/33137782/)
  100. D. Pang et al., Electrochemical actuators based on two-dimensional  $Ti_3C_2T_x$  (MXene). *Nano Lett.* **19**, 7443–7448 (2019). doi: [10.1021/acsnano.9b03147](https://doi.org/10.1021/acsnano.9b03147); pmid: [31536705](https://pubmed.ncbi.nlm.nih.gov/31536705/)
  101. G. Cai, J. H. Ciou, Y. Liu, Y. Jiang, P. S. Lee, Leaf-inspired multiresponsive MXene-based actuator for programmable smart devices. *Sci. Adv.* **5**, eaaw7956 (2019). doi: [10.1126/sciadv.aaw7956](https://doi.org/10.1126/sciadv.aaw7956); pmid: [31309158](https://pubmed.ncbi.nlm.nih.gov/31309158/)
  102. F. Shahzad et al., Electromagnetic interference shielding with 2D transition metal carbides (MXenes). *Science* **353**, 1137–1140 (2016). doi: [10.1126/science.aag2421](https://doi.org/10.1126/science.aag2421); pmid: [27609888](https://pubmed.ncbi.nlm.nih.gov/27609888/)
  103. M. Han et al., Beyond  $Ti_3C_2T_x$ : MXenes for electromagnetic interference shielding. *ACS Nano* **14**, 5008–5016 (2020). doi: [10.1021/acsnano.0c01312](https://doi.org/10.1021/acsnano.0c01312); pmid: [32163265](https://pubmed.ncbi.nlm.nih.gov/32163265/)
  104. A. Iqbal et al., Anomalous absorption of electromagnetic waves by 2D transition metal carbonitride  $Ti_3CNT_x$  (MXene). *Science* **369**, 446–450 (2020). doi: [10.1126/science.aba7977](https://doi.org/10.1126/science.aba7977); pmid: [32703878](https://pubmed.ncbi.nlm.nih.gov/32703878/)
  105. M. Han et al., Solution-processed  $Ti_3C_2T_x$  MXene antennas for radio-frequency communication. *Adv. Mater.* **33**, 2003225 (2021). doi: [10.1002/adma.202003225](https://doi.org/10.1002/adma.202003225)
  106. M. Naguib et al., MXene: A promising transition metal carbide anode for lithium-ion batteries. *Electrochem. Commun.* **16**, 61–64 (2012). doi: [10.1016/j.elecom.2012.01.002](https://doi.org/10.1016/j.elecom.2012.01.002)
  107. M. Okubo, A. Sugahara, S. Kajiyama, A. Yamada, MXene as a charge storage host. *Acc. Chem. Res.* **51**, 591–599 (2018). doi: [10.1021/acs.accounts.7b00481](https://doi.org/10.1021/acs.accounts.7b00481); pmid: [29469564](https://pubmed.ncbi.nlm.nih.gov/29469564/)
  108. M. Q. Zhao et al., Flexible MXene/carbon nanotube composite paper with high volumetric capacitance. *Adv. Mater.* **27**, 339–345 (2015). doi: [10.1002/adma.201404140](https://doi.org/10.1002/adma.201404140); pmid: [25405330](https://pubmed.ncbi.nlm.nih.gov/25405330/)
  109. C. Chen et al.,  $MoS_2$ -on-MXene heterostructures as highly reversible anode materials for lithium-ion batteries. *Angew. Chem. Int. Ed.* **57**, 1846–1850 (2018). doi: [10.1002/anie.201710616](https://doi.org/10.1002/anie.201710616); pmid: [29292844](https://pubmed.ncbi.nlm.nih.gov/29292844/)
  110. X. Li et al., Activating the  $I^{+}/I^-$  redox couple in an aqueous  $I_2-Zn$  battery to achieve a high voltage plateau. *Energy Environ. Sci.* **14**, 407–413 (2020). doi: [10.1039/D0EE03086D](https://doi.org/10.1039/D0EE03086D)
  111. A. VahidMohammadi, A. Hadjikhani, S. Shahbazmohammadi, M. Beidaghi, Two-dimensional vanadium carbide (MXene) as a high-capacity cathode material for rechargeable aluminum batteries. *ACS Nano* **11**, 11135–11144 (2017). doi: [10.1021/acsnano.7b05350](https://doi.org/10.1021/acsnano.7b05350); pmid: [29039915](https://pubmed.ncbi.nlm.nih.gov/29039915/)
  112. S. Zhao et al., Li-ion uptake and increase in interlayer spacing of  $Nb_4C_3$  MXene. *Energy Storage Mater.* **8**, 42–48 (2017). doi: [10.1016/j.ensmat.2017.03.012](https://doi.org/10.1016/j.ensmat.2017.03.012)
  113. J. Song et al., Immobilizing polysulfides with MXene-functionalized separators for stable lithium-sulfur batteries. *ACS Appl. Mater. Interfaces* **8**, 29427–29433 (2016). doi: [10.1021/acsmi.6b09027](https://doi.org/10.1021/acsmi.6b09027); pmid: [27723285](https://pubmed.ncbi.nlm.nih.gov/27723285/)
  114. X. Liang, A. Garsuch, L. F. Nazar, Sulfur cathodes based on conductive MXene nanosheets for high-performance lithium-sulfur batteries. *Angew. Chem. Int. Ed.* **54**, 3907–3911 (2015). doi: [10.1002/anie.201401074](https://doi.org/10.1002/anie.201401074); pmid: [25650042](https://pubmed.ncbi.nlm.nih.gov/25650042/)
  115. X. Liang, Y. Rangom, C. Y. Kwok, Q. Pang, L. F. Nazar, Interwoven MXene nanosheet/carbon-nanotube composites as Li-S cathode hosts. *Adv. Mater.* **29**, 1603040 (2017). doi: [10.1002/adma.201603040](https://doi.org/10.1002/adma.201603040); pmid: [27859697](https://pubmed.ncbi.nlm.nih.gov/27859697/)
  116. X. Guo et al., Boosting sodium storage in two-dimensional phosphorene/ $Ti_3C_2T_x$ , MXene nanoarchitectures with stable fluorinated interphase. *ACS Nano* **14**, 3651–3659 (2020). doi: [10.1021/acsnano.0c00177](https://doi.org/10.1021/acsnano.0c00177); pmid: [32150388](https://pubmed.ncbi.nlm.nih.gov/32150388/)
  117. C. J. Zhang et al., High capacity silicon anodes enabled by MXene viscous aqueous ink. *Nat. Commun.* **10**, 849 (2019). doi: [10.1038/s41467-019-08383-y](https://doi.org/10.1038/s41467-019-08383-y); pmid: [30787274](https://pubmed.ncbi.nlm.nih.gov/30787274/)
  118. M. R. Lukatskaya et al., Ultra-high-rate pseudocapacitive energy storage in two-dimensional transition metal carbides. *Nat. Energy* **2**, 17105 (2017). doi: [10.1038/nenergy.2017.105](https://doi.org/10.1038/nenergy.2017.105)
  119. X. Wang et al., Influences from solvents on charge storage in titanium carbide MXenes. *Nat. Energy* **4**, 241–248 (2019). doi: [10.1038/s41560-019-0339-9](https://doi.org/10.1038/s41560-019-0339-9)
  120. Y.-Y. Peng et al., All-MXene (2D titanium carbide) solid-state microsupercapacitors for on-chip energy storage. *Energy Environ. Sci.* **9**, 2847–2854 (2016). doi: [10.1039/C6EE01717G](https://doi.org/10.1039/C6EE01717G)
  121. Q. Jiang et al., On-chip MXene microsupercapacitors for AC-line filtering applications. *Adv. Energy Mater.* **9**, 1901061 (2019). doi: [10.1002/aenm.201901061](https://doi.org/10.1002/aenm.201901061)
  122. Y. Dong et al., Metallic MXenes: A new family of materials for flexible triboelectric nanogenerators. *Nano Energy* **44**, 103–110 (2018). doi: [10.1016/j.nanoen.2017.11.044](https://doi.org/10.1016/j.nanoen.2017.11.044)
  123. M. Salauddin et al., A novel MXene/ecoflex nanocomposite-coated fabric as a highly negative and stable friction layer for high-output triboelectric nanogenerators. *Adv. Energy Mater.* **11**, 2002832 (2021). doi: [10.1002/aenm.202002832](https://doi.org/10.1002/aenm.202002832)
  124. R. Li, L. Zhang, L. Shi, P. Wang, MXene  $Ti_3C_2$ : An effective 2D light-to-heat conversion material. *ACS Nano* **11**, 3752–3759 (2017). doi: [10.1021/acsnano.6b08415](https://doi.org/10.1021/acsnano.6b08415); pmid: [28339184](https://pubmed.ncbi.nlm.nih.gov/28339184/)
  125. K. H. Lee et al., Ultrasound-driven two-dimensional  $Ti_3C_2T_x$  MXene hydrogel generator. *ACS Nano* **14**, 3199–3207 (2020). doi: [10.1021/acsnano.9b08462](https://doi.org/10.1021/acsnano.9b08462); pmid: [32078295](https://pubmed.ncbi.nlm.nih.gov/32078295/)
  126. L. Ding et al., Oppositely charged  $Ti_3C_2T_x$  MXene membranes with 2D nanofluidic channels for osmotic energy harvesting. *Angew. Chem.* **132**, 8798–8804 (2020). doi: [10.1002/ange.201915993](https://doi.org/10.1002/ange.201915993)
  127. Z. Zhang et al., Mechanically strong MXene/Kevlar nanofiber composite membranes as high-performance nanofluidic osmotic power generators. *Nat. Commun.* **10**, 2920 (2019). doi: [10.1038/s41467-019-10885-8](https://doi.org/10.1038/s41467-019-10885-8); pmid: [31269637](https://pubmed.ncbi.nlm.nih.gov/31269637/)
  128. Z. W. Seh et al., Two-dimensional molybdenum carbide (MXene) as an efficient electrocatalyst for hydrogen evolution. *ACS Energy Lett.* **1**, 589–594 (2016). doi: [10.1021/acsenergylett.6b00247](https://doi.org/10.1021/acsenergylett.6b00247)
  129. G. Gao, A. P. O'Mullane, A. Du, 2D MXenes: A new family of promising catalysts for the hydrogen evolution reaction. *ACS Catal.* **7**, 494–500 (2017). doi: [10.1021/acscatal.6b02754](https://doi.org/10.1021/acscatal.6b02754)
  130. A. D. Handoko et al., Tuning the basal plane functionalization of two-dimensional metal carbides (MXenes) to control hydrogen evolution activity. *ACS Appl. Energy Mater.* **1**, 173–180 (2018). doi: [10.1021/acsma.7b00054](https://doi.org/10.1021/acsma.7b00054)
  131. H. Lind et al., Hydrogen evolution reaction for vacancy-ordered *i*-MXenes and the impact of proton absorption into the vacancies. *Adv. Sustain. Syst.* **5**, 2000158 (2020). doi: [10.1002/adsu.2020000158](https://doi.org/10.1002/adsu.2020000158)
  132. J. Zhang et al., Single platinum atoms immobilized on an MXene as an efficient catalyst for the hydrogen evolution reaction. *Nat. Catal.* **1**, 985–992 (2018). doi: [10.1038/s41929-018-0195-1](https://doi.org/10.1038/s41929-018-0195-1)
  133. T. Y. Ma, J. L. Cao, M. Jaroniec, S. Z. Qiao, Interacting carbon nitride and titanium carbide nanosheets for high-performance oxygen evolution. *Angew. Chem. Int. Ed.* **55**, 1138–1142 (2016). doi: [10.1002/anie.201509758](https://doi.org/10.1002/anie.201509758); pmid: [26629779](https://pubmed.ncbi.nlm.nih.gov/26629779/)
  134. Y. Luo et al., Efficient electrocatalytic  $N_2$  fixation with MXene under ambient conditions. *Joule* **3**, 279–289 (2019). doi: [10.1016/j.joule.2018.09.011](https://doi.org/10.1016/j.joule.2018.09.011)
  135. A. M. Jastrzebska et al., In vitro studies on cytotoxicity of delaminated  $Ti_3C_2$  MXene. *J. Hazard. Mater.* **339**, 1–8 (2017). doi: [10.1016/j.jhazmat.2017.06.004](https://doi.org/10.1016/j.jhazmat.2017.06.004); pmid: [28601597](https://pubmed.ncbi.nlm.nih.gov/28601597/)
  136. H. Lin, S. Gao, C. Dai, Y. Chen, J. Shi, A two-dimensional biodegradable niobium carbide (MXene) for photothermal tumor eradication in NIR-I and NIR-II biowindows. *J. Am. Chem. Soc.* **139**, 16235–16247 (2017). doi: [10.1021/jacs.7b07818](https://doi.org/10.1021/jacs.7b07818); pmid: [29063760](https://pubmed.ncbi.nlm.nih.gov/29063760/)

137. H. Lin, Y. Wang, S. Gao, Y. Chen, J. Shi, Theranostic 2D tantalum carbide (MXene). *Adv. Mater.* **30**, 1703284 (2018). doi: [10.1002/adma.201703284](https://doi.org/10.1002/adma.201703284); pmid: [29226386](https://pubmed.ncbi.nlm.nih.gov/29226386/)
138. Z. Li *et al.*, Surface nanopore engineering of 2D MXenes for targeted and synergistic multitherapies of hepatocellular carcinoma. *Adv. Mater.* **30**, e1706981 (2018). doi: [10.1002/adma.201706981](https://doi.org/10.1002/adma.201706981); pmid: [29663543](https://pubmed.ncbi.nlm.nih.gov/29663543/)
139. K. Rasool *et al.*, Antibacterial activity of  $Ti_3C_2T_x$  MXene. *ACS Nano* **10**, 3674–3684 (2016). doi: [10.1021/acsnano.6b00181](https://doi.org/10.1021/acsnano.6b00181); pmid: [26909865](https://pubmed.ncbi.nlm.nih.gov/26909865/)
140. N. Driscoll *et al.*, Two-dimensional  $Ti_3C_2T_x$  MXene for high-resolution neural interfaces. *ACS Nano* **12**, 10419–10429 (2018). doi: [10.1021/acsnano.8b06014](https://doi.org/10.1021/acsnano.8b06014); pmid: [30207690](https://pubmed.ncbi.nlm.nih.gov/30207690/)
141. B. B. Murphy *et al.*, A gel-free  $Ti_3C_2T_x$ -based electrode array for high-density, high-resolution surface electromyography. *Adv. Mater. Technol.* **5**, 2000325 (2020). doi: [10.1002/admt.202000325](https://doi.org/10.1002/admt.202000325); pmid: [33693054](https://pubmed.ncbi.nlm.nih.gov/33693054/)
142. E. J. Ward *et al.*, 2D titanium carbide ( $Ti_3C_2T_x$ ) in accommodating intraocular lens design. *Adv. Funct. Mater.* **30**, 2000841 (2020). doi: [10.1002/adfm.202000841](https://doi.org/10.1002/adfm.202000841)
143. F. Meng *et al.*, MXene sorbents for removal of urea from dialysate: A step toward the wearable artificial kidney. *ACS Nano* **12**, 10518–10528 (2018). doi: [10.1021/acsnano.8b06494](https://doi.org/10.1021/acsnano.8b06494); pmid: [30257087](https://pubmed.ncbi.nlm.nih.gov/30257087/)
144. Q. Zhao *et al.*, Adsorption of uremic toxins using  $Ti_3C_2T_x$  MXene for dialysate regeneration. *ACS Nano* **14**, 11787–11798 (2020). doi: [10.1021/acsnano.0c04546](https://doi.org/10.1021/acsnano.0c04546); pmid: [32830949](https://pubmed.ncbi.nlm.nih.gov/32830949/)
145. X. Sang *et al.*, In situ atomistic insight into the growth mechanisms of single layer 2D transition metal carbides. *Nat. Commun.* **9**, 2266 (2018). doi: [10.1038/s41467-018-04610-0](https://doi.org/10.1038/s41467-018-04610-0); pmid: [29891836](https://pubmed.ncbi.nlm.nih.gov/29891836/)
146. G. Deysher *et al.*, Synthesis of  $Mo_2VAIC_4$  MAX phase and two-dimensional  $Mo_4VC_4$  MXene with five atomic layers of transition metals. *ACS Nano* **14**, 204–217 (2020). doi: [10.1021/acsnano.9b07708](https://doi.org/10.1021/acsnano.9b07708); pmid: [31804797](https://pubmed.ncbi.nlm.nih.gov/31804797/)
147. C. Xu *et al.*, Large-area high-quality 2D ultrathin  $Mo_2C$  superconducting crystals. *Nat. Mater.* **14**, 1135–1141 (2015). doi: [10.1038/nmat4374](https://doi.org/10.1038/nmat4374); pmid: [26280223](https://pubmed.ncbi.nlm.nih.gov/26280223/)
148. P. Urbankowski *et al.*, 2D molybdenum and vanadium nitrides synthesized by ammoniation of 2D transition metal carbides (MXenes). *Nanoscale* **9**, 17722–17730 (2017). doi: [10.1039/C7NR06721F](https://doi.org/10.1039/C7NR06721F); pmid: [29134998](https://pubmed.ncbi.nlm.nih.gov/29134998/)
149. J. Cao *et al.*, Realization of 2D crystalline metal nitrides via selective atomic substitution. *Sci. Adv.* **6**, eaax8784 (2020). doi: [10.1126/sciadv.aax8784](https://doi.org/10.1126/sciadv.aax8784); pmid: [31950078](https://pubmed.ncbi.nlm.nih.gov/31950078/)
150. T. Zhao, S. Zhang, Y. Guo, Q. Wang,  $Ti_2C$ : A new two-dimensional sheet beyond MXenes. *Nanoscale* **8**, 233–242 (2016). doi: [10.1039/C5NR04472C](https://doi.org/10.1039/C5NR04472C); pmid: [26503155](https://pubmed.ncbi.nlm.nih.gov/26503155/)
151. L. T. Alameda, P. Moradifar, Z. P. Metzger, N. Alem, R. E. Schaak, Topochemical deintercalation of Al from MoAlB: Stepwise etching pathway, layered intergrowth structures, and two-dimensional MBene. *J. Am. Chem. Soc.* **140**, 8833–8840 (2018). doi: [10.1021/jacs.8b04705](https://doi.org/10.1021/jacs.8b04705); pmid: [29906120](https://pubmed.ncbi.nlm.nih.gov/29906120/)
152. L. T. Alameda, C. F. Holder, J. L. Fenton, R. E. Schaak, Partial etching of Al from MoAlB single crystals to expose catalytically active basal planes for the hydrogen evolution reaction. *Chem. Mater.* **29**, 8953–8957 (2017). doi: [10.1021/acs.chemmater.7b02511](https://doi.org/10.1021/acs.chemmater.7b02511)
153. Y. Yu, J. Zhou, Z. Sun, Novel 2D transition-metal carbides: Ultrahigh performance electrocatalysts for overall water splitting and oxygen reduction. *Adv. Funct. Mater.* **30**, 2000570 (2020). doi: [10.1002/adfm.202000570](https://doi.org/10.1002/adfm.202000570)
154. M. Khazaei *et al.*, Novel MB phases and insights into their exfoliation into 2D MBenes. *Nanoscale* **11**, 11305–11314 (2019). doi: [10.1039/C9NR01267B](https://doi.org/10.1039/C9NR01267B); pmid: [31165851](https://pubmed.ncbi.nlm.nih.gov/31165851/)
155. H. Kumar *et al.*, Tunable magnetism and transport properties in nitride MXenes. *ACS Nano* **11**, 7648–7655 (2017). doi: [10.1021/acsnano.7b02578](https://doi.org/10.1021/acsnano.7b02578); pmid: [28558192](https://pubmed.ncbi.nlm.nih.gov/28558192/)
156. M. Khazaei, A. Ranjbar, M. Arai, S. Yunoki, Topological insulators in the ordered double transition metals  $M_2M'C_2$  MXenes ( $M' = Mo, W; M'' = Ti, Zr, Hf$ ). *Phys. Rev. B* **94**, 125152 (2016). doi: [10.1103/PhysRevB.94.125152](https://doi.org/10.1103/PhysRevB.94.125152)
157. H. Weng *et al.*, Large-gap two-dimensional topological insulator in oxygen functionalized MXene. *Phys. Rev. B* **92**, 075436 (2015). doi: [10.1103/PhysRevB.92.075436](https://doi.org/10.1103/PhysRevB.92.075436)
158. N. Xu *et al.*, Zero-dimensional MXene-based optical devices for ultrafast and ultranarrow photonics applications. *Adv. Sci.* **7**, 2002209 (2020). doi: [10.1002/advs.202002209](https://doi.org/10.1002/advs.202002209); pmid: [33240766](https://pubmed.ncbi.nlm.nih.gov/33240766/)
159. Y. I. Jhon *et al.*, Metallic MXene saturable absorber for femtosecond mode-locked lasers. *Adv. Mater.* **29**, 1702496 (2017). doi: [10.1002/adma.201702496](https://doi.org/10.1002/adma.201702496); pmid: [28714145](https://pubmed.ncbi.nlm.nih.gov/28714145/)
160. K. Rasool *et al.*, Water treatment and environmental remediation applications of two-dimensional metal carbides (MXenes). *Mater. Today* **30**, 80–102 (2019). doi: [10.1016/j.mattod.2019.05.017](https://doi.org/10.1016/j.mattod.2019.05.017)
161. V. Kamysbayev *et al.*, Colloidal gelation in liquid metals enables functional nanocomposites of 2D metal carbides (MXenes) and lightweight metals. *ACS Nano* **13**, 12415–12424 (2019). doi: [10.1021/acsnano.9b06207](https://doi.org/10.1021/acsnano.9b06207); pmid: [31560851](https://pubmed.ncbi.nlm.nih.gov/31560851/)
162. J. Guo *et al.*, Cold sintered ceramic nanocomposites of 2D MXene and zinc oxide. *Adv. Mater.* **30**, e1801846 (2018). doi: [10.1002/adma.201801846](https://doi.org/10.1002/adma.201801846); pmid: [29944178](https://pubmed.ncbi.nlm.nih.gov/29944178/)
163. F. Bian, L. Sun, L. Cai, Y. Wang, Y. Zhao, Bioinspired MXene-integrated colloidal crystal arrays for multichannel bioinformation coding. *Proc. Natl. Acad. Sci. U.S.A.* **117**, 22736–22742 (2020). doi: [10.1073/pnas.2011660117](https://doi.org/10.1073/pnas.2011660117); pmid: [32868413](https://pubmed.ncbi.nlm.nih.gov/32868413/)
164. B. Lyu *et al.*, 2D MXene-TiO<sub>2</sub> core-shell nanosheets as a data-storage medium in memory devices. *Adv. Mater.* **32**, e1907633 (2020). doi: [10.1002/adma.201907633](https://doi.org/10.1002/adma.201907633); pmid: [32187736](https://pubmed.ncbi.nlm.nih.gov/32187736/)
165. H. Wei *et al.*, Redox MXene artificial synapse with bidirectional plasticity and hypersensitive responsibility. *Adv. Funct. Mater.* **31**, 2007232 (2021). doi: [10.1002/adfm.202007232](https://doi.org/10.1002/adfm.202007232)
166. C. E. Shuck *et al.*, Scalable synthesis of  $Ti_3C_2T_x$  MXene. *Adv. Eng. Mater.* **22**, 1901241 (2020). doi: [10.1002/adem.201901241](https://doi.org/10.1002/adem.201901241)
167. S. Uzun *et al.*, Additive-free aqueous MXene inks for thermal inkjet printing on textiles. *Small* **17**, 2006376 (2021). doi: [10.1002/smll.202006376](https://doi.org/10.1002/smll.202006376)
168. J. Lipton *et al.*, Scalable, highly conductive, and micropatternable MXene films for enhanced electromagnetic interference shielding. *Matter* **3**, 546–557 (2020). doi: [10.1016/j.matt.2020.05.023](https://doi.org/10.1016/j.matt.2020.05.023)
169. B. Xu *et al.*, Ultrathin MXene-micropattern-based field-effect transistor for probing neural activity. *Adv. Mater.* **28**, 3333–3339 (2016). doi: [10.1002/adma.201504657](https://doi.org/10.1002/adma.201504657); pmid: [26924616](https://pubmed.ncbi.nlm.nih.gov/26924616/)
170. A. Levitt *et al.*, 3D knitted energy storage textiles using MXene-coated yarns. *Mater. Today* **34**, 17–29 (2020). doi: [10.1016/j.mattod.2020.02.005](https://doi.org/10.1016/j.mattod.2020.02.005)
171. H. Lin, X. Wang, L. Yu, Y. Chen, J. Shi, Two-dimensional ultrathin MXene ceramic nanosheets for photothermal conversion. *Nano Lett.* **17**, 384–391 (2017). doi: [10.1021/acs.nanolett.6b0439](https://doi.org/10.1021/acs.nanolett.6b0439); pmid: [28026960](https://pubmed.ncbi.nlm.nih.gov/28026960/)

**ACKNOWLEDGMENTS**

**Funding:** Y.G. and A.V.M. acknowledge support from the Fluid Interface Reactions, Structures, and Transport (FIRST) Center, an Energy Frontier Research Center funded by the US Department of Energy, Office of Science, and Office of Basic Energy Sciences for MXene electrochemistry research. Search for new MXene compositions by Y.G. was also supported by National Science Foundation awards DMR-2041050 and DMR-2035007. J.R. acknowledges funding from the Knut and Alice Wallenberg (KAW) Foundation and the Swedish Foundation for Strategic Research (SSF). The Swedish Government Strategic Research Area in Materials Science on Functional Materials at Linköping University (Faculty Grant SFO Mat Liu No. 2009 00971) is also acknowledged. **Competing interests:** None declared.

10.1126/science.abf1581